THEORETICAL BIOLOGY FORUM
ISSN: 2283-7175 | https://tbfpeerjournal.org/

Advanced Surface Complexation Modeling of Arsenic Adsorption onto TiO_2/Fe_2O_3 Sorbents: Relevance to Human Exposure Reduction and Health Risk Mitigation

Dr. J. C. Bellamy[1]*, Dr. J. P. L. Kenward[2], Dr. S. Farrow[3], Dr. A. Kafiros[4], Dr. S. Skinner[3], Prof. D. J. Weissberg[1,5]*

[1] Department of Clinical Medicine and Translational Research, University of Oxford, Oxford OX3 7LF, United Kingdom

[2] Department of Biomedical Sciences, Faculty of Health, University of Ottawa, Ottawa, Ontario K1N 6N5, Canada

[3] Department of Materials Science in Medicine, Imperial College London, London SW7 2AZ, United Kingdom

[4] Department of Medicinal Chemistry, White City Campus, Imperial College London, London W12 0BZ, United Kingdom

[5] Department of Environmental Health and Epidemiology, Princeton University, Princeton, New Jersey 08544, United States

Keywords

arsenic; adsorption; TiO_2; iron oxide; composite; surface complexation model; SCM; low energy ion scattering; LEIS; surface analysis

Graphical abstract

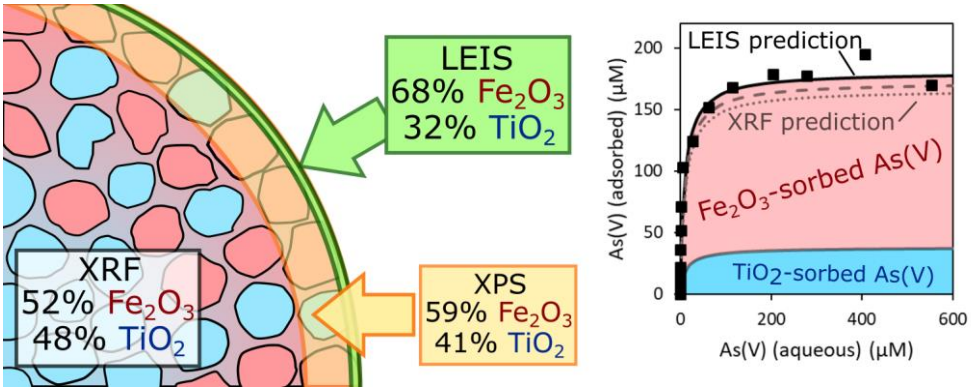

Abstract

Many novel composite materials have been recently developed for water treatment applications, with the aim of achieving multifunctional behaviour, e.g. combining adsorption with light-driven remediation. The application of surface complexation models (SCM) is important to understand how adsorption changes as a function of pH, ionic strength and the presence of competitor ions. Component additive (CA) models describe composite sorbents using a combination of single-phase reference materials. However, predictive adsorption modelling using the CA-SCM approach remains unreliable, due to challenges in the quantitative determination of surface composition. In this study, we test the hypothesis that characterisation of the outermost surface using low energy ion scattering (LEIS) improves CA-SCM accuracy. We consider the TiO_2/Fe_2O_3 photocatalyst-sorbents that are increasingly investigated for arsenic remediation. Due to an iron oxide surface coating that was not captured by bulk analysis, LEIS significantly improves the accuracy of our component additive predictions for monolayer surface processes: adsorption of arsenic(V) and surface acidity. We also demonstrate non-component additivity in multilayer arsenic(III) adsorption, due to changes in surface morphology/porosity. Our results demonstrate how surface-sensitive analytical techniques will improve adsorption modelling for the next generation of composite sorbents.

1. Introduction

Adsorption onto low-cost materials is well established as an effective method for the removal of toxic metals and metalloids from contaminated water [1]. Current efforts to improve water treatment include the development of new composite sorbents, either to improve adsorption kinetics and capacity [2], or to impart new functionality. Multifunctional sorbents combine adsorption with other properties such as magnetism, for the easy separation of clean water from sludge [3 4], or photocatalytic activity, to oxidise arsenite; reduce chromate; or degrade organic matter [5 6 7].

Surface complexation models (SCM) are powerful tools to help understand the behaviour of new sorbents. SCMs predict adsorption as a function of pH, ionic strength, and the presence of competitor ions, thereby offering sensitivity to environmental conditions that is missing in the more widely used Langmuir and Freundlich models [8]. Surface complexation models are well established for homogeneous sorbents with a single solid phase, but two contrasting approaches are used to model heterogeneous sorbents with multiple solid phases: the generalised component (GC) and component additive (CA) methods.

The GC method approximates and models the heterogeneous sorbent as a homogeneous, single-component surface [9 10]. This is the more common approach, but has notable limitations. Firstly, this model cannot predict how adsorption will change as the distribution between solid phases changes, since equilibrium constants are unique to each sorbent sample [9]. GC models will therefore fail when synthetic sorbents are prepared under different conditions, or natural sorbents are sampled from different locations. Secondly, adsorption onto different surface phases is convoluted, limiting our insight into how the sorbate partitions between the different solid phases composing the overall sorbent [11].

The CA method describes the heterogeneous sorbent as a combination of distinct surface components, each with its own adsorption equilibrium constants. Normally, each surface component is assigned to a single-phase reference material. Unlike the GC approach, component additive modelling has advantages in that (i) CA models are easily adjusted to predict adsorption onto new samples with different distributions between solid phases, and (ii) CA modelling provides insights into how the sorbate partitions between each surface component [12]. However, the CA-SCM approach has had mixed success in describing experimental results, with the main challenge being the accurate quantification of how much each component contributes to the overall sorbent surface area [9].

Most previous studies have used the mass ratio of phases within the bulk material to weight the contribution of each component within the CA-SCM [13 14 15 16 17 18 19]. This approach assumes that the bulk composition of the sorbent material reflects the surface composition. This assumption often leads to errors, e.g. in scenarios where (a) particles of one component are smaller than the other and thus exhibit a higher surface area-to-mass ratio, or (b) one component is a surface coating, blocking adsorption onto the second component [9]. Secondary minerals such as amorphous iron and aluminium (hydr)oxides are examples of high surface area-to-mass ratio coatings common in natural samples [9]. For these reasons, the mass-weighted component additive approach often fails to describe experimental observations [13 20 17]. The errors of mass-weighted CA-SCM can be very large, e.g. an underestimation of ca. 51% in the adsorption of uranium(VI) onto phyllite [13]; errors between -50% and +300% in the adsorption of Cu(II) onto ferrihydrite-bacteria composites [17]; and errors of -30% to +80% in the adsorption of Cu(II) onto montmorillonite-bacteria composites [20]. In these cases, equilibrium constants are often re-optimised to fit experimental adsorption data collected using the composite material [17]. Consequently, the advantages that CA-SCM has over GC-SCM are lost. X-ray diffraction (XRD) has also been used for weighting components [21 22 23], however X-rays are highly penetrating and XRD-weighting thus shares the same problems as mass-weighting.

A few experimental techniques have been used to quantify the composition of the sorbent surface and improve CA-SCM component weighting. These are (a) chemical extractions [9 24], and (b) the fitting of experimental adsorption isotherms against single-component reference isotherms [25]. Chemical extractions can be used to quantify the abundance of a surface coating when the solid phase is different to the bulk material. However, this technique has poor surface sensitivity, especially for thick coatings, and the technique is inaccurate when strong treatments dissolve the bulk material [9]. Meanwhile, whilst providing a very good CA-SCM fit for uranium(VI) adsorption onto natural sediments, Dong and Wan noted that their approach of fitting adsorption isotherms is limited to binary sorbents, and more complex ternary systems cannot be weighted using this approach alone [25]. Several authors have commented on how new surface characterisation techniques are needed to improve the accuracy of predictions made through component additive modelling [10 24].

Surface-sensitive analytical techniques are increasingly available and offer solutions to problems of accuracy, surface-sensitivity, and challenging ternary systems. However, the application of these techniques for developing CA-SCMs remains untested. For instance, X-ray photoelectron spectroscopy (XPS) is now routinely used to investigate the near-surface (1-10 nm [26]) of materials, before and after adsorption [27]. Despite being a quantitative

technique, we found no previous study using XPS to weight components within CA models. Another, albeit less widely applied technique is low energy ion scattering (LEIS), a spectroscopic technique sensitive to the outermost atomic surface of a material [28 29 30]. XPS and LEIS provide distinct peaks for each element, resolved on the basis of electron binding energy and atomic mass respectively [31 32], and can therefore characterise the ternary composite sorbents [33] that cannot be understood by adsorption isotherms alone [25]. To date, no study has used LEIS for modelling multicomponent adsorption. This work therefore tests the hypothesis that CA-SCM accuracy is improved by choosing surface-sensitive characterisation techniques, with a focus on LEIS.

As the system of interest, we considered adsorption of arsenic onto TiO_2/Fe_2O_3 composites. Inorganic As(III) (arsenite) is a carcinogenic contaminant prevalent in the reducing groundwaters of South Asia, with tens of millions of people exposed [34]. The dominant species of As(III) in groundwater is H_3AsO_3 which, due to its neutral charge, is difficult to remove from drinking water. A number of research groups have explored the application of bifunctional photocatalyst-sorbents, whereby As(III) is photocatalytically oxidised to As(V) and then adsorbed. As(V) is less toxic than As(III), and its negatively charged oxyanions ($HAsO_4^{-2}$ and $H_2AsO_4^-$) are more easily removed. The most popular photocatalyst-sorbents are TiO_2/Fe_2O_3 composites [5 6 35 3]. These combine titania (TiO_2), the benchmark photocatalyst [36], with iron oxides such as goethite (FeOOH) and hematite (Fe_2O_3), which are used commercially as As(V) sorbents [37]. Our research group has identified the mesoporous TiO_2/Fe_2O_3 composite described by Zhou *et al.* as a promising multifunctional sorbent for As(III) remediation, combining high adsorption capacities with fast photocatalytic oxidation rates when irradiated with ultraviolet light [5 38].

An accurate CA-SCM for the TiO_2/Fe_2O_3 system is a desirable tool for two reasons. Firstly, adsorption of arsenic onto these materials is poorly understood, e.g. whether the TiO_2 and Fe_2O_3 surfaces behave independently, or whether new chemistry arises once the materials are coupled. Previous work towards understanding arsenic adorption in mixed sorbent systems is limited [39]. An accurate CA-SCM will improve our understanding of how arsenic partitions across the composite sorbent surface. Secondly, an accurate CA model will predict the influence of surface composition (*i.e.* the TiO_2:Fe_2O_3 ratio) on arsenic adsorption, allowing the synthesis of meso-TiO_2/Fe_2O_3 to be optimised for improved performance.

The aim of this work was to use surface-sensitive analytical techniques to develop an accurate CA-SCM that quantifies the adsorption of arsenic onto mesoporous TiO_2/Fe_2O_3. The material composition of meso-TiO_2/Fe_2O_3 before adsorption of arsenic was calculated in the bulk (X-ray fluorescence, XRF), at the near surface (XPS), and at the outermost surface (LEIS). These results were used to constrain the relative abundance of meso-TiO_2 and Fe_2O_3 surface components, under the hypothesis that LEIS analysis would provide the most accurate component additive model, owing to its superior surface sensitivity. XPS was chosen as it is a more widely available technique. XRF was chosen to represent how the mass ratio has been used to weight surface components in most previous studies. We investigated the accuracy of CA models weighted by these three different techniques by predicting the following chemical behaviour: (a) surface charge (determined by potentiometric titration); (b) arsenic(V) adsorption (using the Langmuir isotherm); and (c) arsenic(III) adsorption (using the Freundlich isotherm). Finally, we developed a CA-SCM by experimentally determining SCM parameters for single-component reference sorbents, and assessed how the choice of characterisation technique influences the accuracy of CA-SCM predictions. Throughout this study Bayoxide E33, a synthetic goethite (FeOOH), was used as a benchmark sorbent to validate our work against that of Kanematsu *et al.* [40 41].

2. Materials and Methods

2.1. Synthesis of meso-TiO_2/Fe_2O_3 and reference samples

All chemicals were at least reagent grade with full details given in the Supplementary Information. Meso-TiO_2 was prepared by a sol-gel synthesis [42]. Firstly, P123 (1 g, PEG Pluronic® P-123, Aldrich) was dissolved in ethanol (12 g, VWR, ACS Puriss p.a. grade). This solution was slowly added to a second solution, consisting of Ti(IV) n-butoxide (2.7 g, ACROS Organics, 99% purity) dissolved in 37% hydrochloric acid (3.2 g, ACROS Organics, ACS reagent grade). The mixture was stirred and aged at room temperature for approximately one week. A solid powder was obtained after calcination (350 °C, 4 hours, 1 °C min^{-1} ramping) and crushed by pestle and mortar. An aliquot of the meso-TiO_2 product was kept as a reference sample.

Meso-TiO_2 was then coupled with Fe_2O_3 [5]. Firstly, a 0.6 M solution of ethanolic $Fe(NO_3)_3.9H_2O$ (Sigma-Aldrich, ACS reagent grade, ≤98% purity) was prepared. Meso-TiO_2 was added to this solution (1.5 g in 30 mL), which was stirred (30 minutes), sonicated (30 minutes), and dried in an oven (50 °C) until all solvent had evaporated. The product was calcinated at 300 °C for 10 minutes, crushed, and calcinated again at 300 °C for 6 hours. Based upon the mass of reagents used, the theoretical mass ratio of meso-TiO_2 and Fe_2O_3 within the meso-TiO_2/Fe_2O_3 composite was 50:50.

A reference sample of Fe_2O_3 was synthesised using the same procedure, but without addition of meso-TiO_2. A sample of FeOOH (goethite, Bayoxide E33) was obtained commercially. Bayoxide E33 is a high surface area goethite, and is a commercially established sorbent for arsenic remediation [43].

All mineral powders were washed in dialysis tubing for 18 days, by which point the pH reading of the wash water had stabilised. Irreversibly consumed acid impurities were completely removed from meso-TiO_2 during washing, but incompletely from Fe_2O_3-containing samples. The FeOOH sample did not have net acid/base impurities before or after washing (Supplementary Information).

Stock solutions of As(V) and As(III) in Milli-Q water (1000 mg L^{-1}) were prepared from $Na_2HAsO_4 \cdot 7H_2O$ (Sigma, ACS reagent grade) and As_2O_3 (Aldrich, 99% purity) respectively. As(III) solutions were stored in opaque plastic bottles to prevent photooxidation. All stock solutions were kept refrigerated (3 °C) and replaced every few weeks. Stock solutions were calibrated against a standard solution of arsenic (1000 ± 4 mg L^{-1}, Fluka, TraceCERT grade) using inductively coupled plasma mass spectrometry (ICP-MS).

2.2. Materials characterisation

Crystal phases were confirmed by X-ray diffraction (XRD) using the PANalytical MPD, and crystallite diameters were estimated using the Scherrer equation (Supplementary Information). Aggregate particles were studied by scanning electron microscopy (SEM) using the LEO Gemini 1525 FEGSEM, and the constituent crystallites were studied by transmission electron microscopy (TEM) and scanning transmission electron microscopy coupled with energy dispersive X-ray spectroscopy (STEM-EDS) using the JEOL JEM-2100F. N_2 adsorption-desorption isotherms were obtained using the Quantachrome Autosorb iQ, outgassing FeOOH at 100 °C and all other samples at 200 °C, for 20 hours. The N_2 adsorption branch was used to determine the surface area and total pore volume using Brunauer-Emmett-Teller (BET) analysis, and the desorption branch was used to determine pore size using Barrett-Joyner-Halenda (BJH) analysis.

The relative abundance of meso-TiO_2 and Fe_2O_3 components within meso-TiO_2/Fe_2O_3 was quantified by: (i) X-ray fluorescence (XRF, for the bulk composition) using the PANalytical Epsilon 3 XLE; (ii) X-ray photoelectron spectroscopy (XPS, for the near surface composition) using the Thermo Scientific K-alpha system; and (iii) low energy ion scattering (LEIS) using the combined IONTOF TOF.SIMS^5-Qtac^{100} LEIS instrument (for the outermost surface composition). The peak area was used for quantification in all three techniques. All samples were characterised before adsorption of arsenic only.

XRF analysis was carried out under the standard Omnian settings (PANalytical Omnian software).

Before XPS analysis, samples were oven dried overnight (70 °C for FeOOH and 200 °C for all other samples) to remove adsorbed water and carbonate. Spectra were recorded for the C1s, O1s, Fe2p and Ti2p regions, using the Al Kα line at 1486.6 eV with a line-width of 0.85 eV and a spot size of 400 μm^2, with the flood gun switched on. XPS data was analysed using Thermo Avantage software, with the C1s adventitious carbon peak normalised to 284.8 eV.

Before LEIS analysis, samples were pumped down to vacuum overnight to remove water. LEIS survey spectra were obtained using He^+ 3 keV and Ne^+ 5 keV primary beams, rastering over a 1 mm^2 area. A LEIS depth profile was carried out in order to remove adsorbed organic carbon which obscured the metal peaks (particularly Ti). Depth profiles were obtained using the Ne^+ primary beam and the Ar^+ sputter gun (0.5 keV, 100 nA, 2mm^2, 15 s) with a one second pause for discharge using the flood gun. Depth profiling was performed until surface impurities had been removed and the area of the metal peaks no longer increased.

For each technique, the contribution of meso-TiO_2 and Fe_2O_3 components to the overall meso-TiO_2/Fe_2O_3 composite was determined (in the bulk, at the near surface, or at the outermost surface) using the formula:

$$m(a)_{composite} = \frac{I(a)_{composite}}{I(a)_A} \div \left(\frac{I(a)_{composite}}{I(a)_A} + \frac{I(b)_{composite}}{I(b)_B} \right)$$

Equation 1

where *a* is the component of interest (i.e. Fe_2O_3 or meso-TiO_2) and *b* is the second component (*i.e.* meso-TiO_2 or Fe_2O_3), A and B are the reference samples (defined as being composed of 100% component *a* and *b* respectively), m(*a*) is the mass fraction of component *a*, and I(*i*) is the intensity (counts) of component *i* within the spectrum. The denominator (in brackets) ensures that the combined mass fractions of all components equals unity. For ternary systems, further quotients for components C, D, E, etc. are added inside the brackets of the denominator.

When processing XRF data, impurities were <1% of the total atomic weight and were ignored. When processing XPS data, Fe and Ti peaks were scaled to account for absorption of the incident beam by impurities (carbon, nitrogen and chlorine) which varied across samples. No impurity correction was needed for LEIS analysis. For all three techniques, uncertainties in the quantitative composition of meso-TiO_2/Fe_2O_3 were calculated as the difference between (a) the combined intensity of Fe and Ti peaks (relative to each reference peak), and (b) the theoretical combined intensity (equal to unity). The expression used is:

$$error\ (\%) = \left| 100 \times \left(\frac{I(a)_{composite}}{I(a)_A} + \frac{I(b)_{composite}}{I(b)_B} - 1 \right) \right|$$

Equation 2

XRF analysis required 30 minutes per sample, XPS required 30-60 minutes per sample, and a single day of LEIS analysis was used to depth profile all samples.

Surface charge as a function of pH was determined by potentiometric titration, and was used both to provide the SCM with experimental electrostatic data, and to check for component additivity. A titration procedure was developed in line with the recommended conditions of Lützenkirchen *et al.* [44], using the Metrohm 888 Titrando and pH electrode. Mineral suspensions (10 g L^{-1}) were titrated in 0.01, 0.05 and 0.1 M NaCl to identify the point of zero salt effect (pzse) as a primary measure of the point of zero charge (pzc). Suspensions were first acidified to pH 3-4 with 0.1 M HCl and bubbled with N_2 gas for two hours to purge the system of carbonate. Suspensions were then titrated forwards to pH 10-11 using 0.1 M NaOH, followed by a reverse titration using 0.1 M HCl to check for hysteresis. Titrations were carried out over 7 hours in both forwards (base) and reverse (acid) directions, and showed good reversibility with low hysteresis (Supplementary Information). The electrode potential (mV) was converted to pH using a 4 point calibration curve with buffer solutions at pH 4, 7, 10 and 13. Buffer solutions and mineral suspensions were kept at 25.0 °C using a water bath. The titrant concentration was calibrated against a standard solution of 1.000 M HCl. For titrations in 0.1 M NaCl, ionic strength dropped by around 3% over the course of the forward titration. In 0.01 M NaCl, ionic strength increased by up to 14% during the forward titration. This was accounted for in the modelling, by explicitly defining the ionic strength at each titration step, and using the Davies equation (valid up to 0.5 M ionic strength) to calculate activity coefficients [45]. The surface area of the sorbent in the vessel was typically above 30 m^2. The pzse was determined as the intersection of titration curves in 0.01, 0.05 and 0.1 M NaCl. Surface charge was calculated as the net proton excess using:

$$Q = c(a)\text{-}c(b)\text{-}([H^+]\text{-}[^-OH])$$

Equation 3

where Q is the surface proton excess (M); c(a) and c(b) are the total amounts of acid and base added to the system respectively (M); and $[H^+]$ and $[^-OH]$ (M) were determined from the measured pH, using the Davies equation. The influence of acidic impurities within each sample was countered by subtracting the value of Q at the pzse from all data points within each titration.

Dynamic light scattering (DLS) was used to determine particle size and zeta potential (and thus the isoelectric point, iep). Powders (1 g L^{-1}) were suspended in 0.01 M NaCl and the pH was adjusted with small additions of 1 and 0.01 M HCl or NaOH. Suspensions were equilibrated for two days before the final pH was recorded and suspensions were analysed using the Malvern Zetasizer Nano. The iep was determined as the pH where samples exhibited zero zeta potential.

2.3. Arsenic adsorption isotherms and pH edges

Adsorption batch experiments were conducted with 1 g L^{-1} sorbent suspended in 0.01 M NaCl and spiked with arsenic. The pH was adjusted with small additions of 0.01 or 1 M HCl and NaOH. Suspensions were shaken for two hours to condition the surface before being spiked with As(V) or As(III) (50 mL total volume). As(III) suspensions were prepared in opaque containers and kept in the dark, to prevent oxidation in the presence of TiO_2 [46 47]. For the pH adsorption edge, total As was fixed at 0.3 mM and the pH was varied between 3 and 11. For the adsorption isotherm, pH was fixed at 7.0 ±0.1 and the concentration of aqueous As was varied between 0.1 and 700 µM. In all batch experiments, the pH was adjusted over the course of several days with small aliquots of 0.01 and 1 M HCl and NaOH, and suspensions were equilibrated for 5 days with continuous shaking before a final pH measurement was taken [6 40]. Suspensions were filtered (0.45 µm, nylon mesh), and the aqueous filtrate was acidified to 2% HNO_3 by mass before total As was determined using the Agilent 7900 quadrupole inductively coupled plasma mass spectrometer (ICP-MS). Results were calibrated using internal standards and a matrix-matched external calibration curve of at least 5 points (1000 ± 4 mg L^{-1}, Fluka standard As, TraceCERT) covering the experimental range. Blank electrolytes, blank mineral suspensions, and matrix-matched arsenic control samples were analysed by ICP-MS in parallel with each batch.

Arsenic adsorption isotherms were modelled using the Langmuir and Freundlich equations:

$$q_e = q_{max}(K_L C_e/(1 + K_L C_e))$$

Equation 4: the Langmuir adsorption isotherm

$$q_e = K_F {C_e}^{1/n}$$

Equation 5: the Freundlich adsorption isotherm

where q_e is the equilibrium concentration of adsorbed arsenic (µmol m^{-2}); q_{max} is the amount adsorbed at monolayer coverage (µmol m^{-2}); C_e is the equilibrium concentration of aqueous arsenic (µM); and K_L (μM^{-1}), K_F (µmol m^{-2} $\mu M^{-1/n}$) and n (dimensionless) are all experimentally determined constants [6].

2.4. Component additive predictions

Component additive predictions for the surface charge and arsenic adsorption of meso-TiO_2/Fe_2O_3 were calculated using a linear combination of the meso-TiO_2 and Fe_2O_3 single-component reference samples, using the following formula:

$$P_{composite} = m_A P_A + m_B P_B$$

Equation 6

where P_i represents the chemical property of material *i* under a given set of experimental conditions (pH, ionic strength, aqueous arsenic concentration), and m_i represents the relative abundance (mass fraction) of component *i*, calculated using Equation 1. In this study, the chemical properties investigated using the component additive approach were (a) net proton excess/surface charge, (b) the concentration of As(V) adsorbed, and (c) the concentration of As(III) adsorbed. For all chemical properties, linear combinations were calculated using XRF-, XPS- and LEIS-weighted values of m_i. Ternary composites can be easily modelled by incorporation of further $m_i P_i$ terms where *i* corresponds to components C, D, E… etc.

2.5. Surface Complexation Modelling

Surface complexation model (SCM) parameters were obtained for each single-component reference sorbent using the extended triple layer model (ETLM) and a method described by Kanematsu *et al.* [41], wherein (i) the site density of each mineral (surface hydroxyls per square nanometre) is chosen from the literature; (ii) equilibrium constants for surface hydroxyl (de)protonation are predicted using Sverjensky's empirical formula [48]; (iii) electrolyte adsorption constants (and inner-sphere capacitance, C_1) are determined by fitting experimental potentiometric titration data; and (iv) arsenic surface complexation constants are determined by fitting pH adsorption edges [49 41]. The SCM parameters were then validated by using the SCM to predict adsorption isotherms, which were compared against experimental observations [41]. Further details are given in the Supplementary Information.

Since Fe_2O_3 showed a similar maximum As(V) adsorption capacity to FeOOH (when normalised to surface area), the site density of both iron oxides was set to 4.0 sites nm^{-2} as per previous studies on Bayoxide E33 [40]. The site density of meso-TiO_2 was set to 3.0 sites nm^{-2} as per Jonsson *et al.* [50]. The outer capacitance (C_2) was set to 0.2 F m^{-2} as per common practice [51 48]. The difference between the acidity constants $\log K0_1$ and $\log K0_2$ (labelled ΔpK_n^{θ}) was set to 5.6 for the iron oxides [41 51] and 6.3 for meso-TiO_2 [52 51]. These values of ΔpK_n^{θ} were previously calculated using analysis of titration data, and Born solvation/crystal chemistry theory [53 51].

Acidity constants were calculated as follows:

Equation 7

$$>SOH + H^+ \rightleftharpoons >SOH_2^+$$

$$\log K_1^{\theta} = pH_{pzc} - \frac{\Delta pK_n^{\theta}}{2}$$

$$\log K_1^{0} = \log K_1^{\theta} - \log\left(\frac{N_S A_S}{N^{\ddagger} A^{\ddagger}}\right)$$

Equation 8

$$>SO^- + H^+ \rightleftharpoons >SOH$$

$$\log K_2^{\theta} = pH_{pzc} + \frac{\Delta pK_n^{\theta}}{2}$$

$$\log K_2^{0} = \log K_2^{\theta} + \log\left(\frac{N_S A_S}{N^{\ddagger} A^{\ddagger}}\right)$$

where >SOH denotes a surface hydroxyl, pH_{pzc} is the pH at the point of zero charge (set to the pzse), θ denotes equilibrium constants for the site-occupancy standard state, and 0 denotes the hypothetical 1.0 M standard state equilibrium constants entered into FITEQL [51]. N_s and A_s are the site densities and BET-specific surface areas used in FITEQL respectively, whilst $N^{\ddagger}$ and $A^{\ddagger}$ refer to the site density and surface area of the site-occupancy standard state (set as 10 sites nm^{-2} and 10 m^2 g^{-1}) [51].

The ETLM incorporates explicit reactions for electrolyte adsorption, which help determine the surface charge. Equilibrium constants for the adsorption of Na^+ and Cl^- ($K0_M$ and $K0_L$ respectively) were determined by fitting potentiometric titrations, with the following reactions:

$$>SOH + Na^+ \rightleftharpoons >SO^-Na^+ + H^+$$

Equation 9

$$>SOH + H^+ + Cl^- \rightleftharpoons >SOH_2^+Cl^-$$

Equation 10

Changes in sorbent concentration and ionic strength during the course of the titration were included in all calculations. The inner capacitance (C_1) was obtained by optimising the SCM fit to potentiometric titration data. For each sample, the three values of $\log K0_M$ and $\log K0_L$, optimised using titrations in 0.01, 0.05 and 0.1 M NaCl, were combined as a single average, to be used in subsequent arsenic adsorption models.

Equilibrium constants for the aqueous speciation of As(V) and As(III) were taken from Dixit and Hering [54 55]. Arsenic surface complexation constants were determined by fitting pH adsorption edges. The sorbent-arsenic

surface complexes used by Kanematsu to describe arsenic adsorption over FeOOH were selected as a starting point, as these complexes (a) were based upon spectroscopic evidence, (b) gave a good fit to experimental pH adsorption edges, and (c) successfully predicted adsorption isotherms at low concentration (before surface precipitation occurrs) [41] [40]. For the adsorption of As(V), the surface complexation reactions modelled were:

$$2\ {>}SOH + H_3AsO_4 \rightleftharpoons (>SO)_2AsO_2^- + H^+ + 2H_2O$$

Equation 11

$$2\ {>}SOH + H_3AsO_4 \rightleftharpoons (>SO)_2AsO_2H + 2H_2O$$

Equation 12

$$>SOH + H_3AsO_4 \rightleftharpoons >SOAsO_3^{2-} + 2H^+ + H_2O$$

Equation 13

and for the adsorption of As(III):

$$2\ {>}SOH + As(OH)_3 \rightleftharpoons (>SO)_2AsO^- + H^+ + 2H_2O$$

Equation 14

$$2\ {>}SOH + As(OH)_3 \rightleftharpoons (>SO)_2AsOH + 2H_2O$$

Equation 15

$$>SOH + As(OH)_3 \rightleftharpoons >SOH_2^+\text{---}AsO(OH)_2^-$$

Equation 16

where the dashed line represents a hydrogen bond.

Finally, an equilibrium constant for multilayer adsorption was included to account for the difference between (i) the experimentally observed, and (ii) the SCM-predicted adsorption of As(III) onto each reference material (FeOOH, Fe_2O_3 and meso-TiO_2). Multilayer adsorption was modelled using the reaction:

$$(>SO)_2AsOX + As(OH)_3\ (aq) \rightleftharpoons \tfrac{1}{2}\ As_2O_3\ (s) + (>SO)_2AsOX + 3/2\ H_2O\ (l)$$

Equation 17

where X is either a proton or a single negative charge; the mass action is equal to the product of the activity of $As(OH)_3$ (aq) and the sum of the activities of $(>SO)_2AsO^-$ and $(>SO)_2AsOH$ surface complexes; and the mass balance is equal to $As(OH)_3$ (aq) only (i.e. there is no net consumption of surface complexes, they act to catalyse the process of precipitation). Equilibrium constants for this reaction were obtained by optimising the SCM fit to the adsorption isotherms. The monodentate H-bonded complex did not provide sites for multilyer adsorption within this model.

All SCM modelling and fitting was performed using FITEQL 2.0 [56], with reference input files provided elsewhere [57]. The charge balance of each complex and the mathematical relationships between logK0 and logKθ are given in the Supplementary Information.

3. Results and Discussion

In this study, we aimed to use surface-sensitive analytical techniques to develop a CA-SCM that describes the adsorption of arsenic onto meso-TiO_2/Fe_2O_3, by accurately quantifying the contribution of each sorbent phase. The structure of the composite sorbent was first investigated, and the distribution between meso-TiO_2 and Fe_2O_3 phases was quantified, both in the bulk material and at the surface. Secondly, surface charge and arsenic adsorption were investigated using the component additive approach. For each reference sample, pH adsorption edges were used to determine surface complexation constants. Finally, LEIS was used to weight meso-TiO_2 and Fe_2O_3 components within the CA-SCM, and the accuracy was evaluated by comparing the adsorption isotherms predicted by CA-SCM against experimental observations. Raw data sets, data processing templates and examples of FITEQL input and output files are available elsewhere [57].

3.1. Characterisation of the meso-TiO_2/Fe_2O_3 composite and reference samples

XRD confirmed the crystal structures of goethite (α-FeOOH) and hematite (α-Fe_2O_3) powders. Rutile gave the most intense of the TiO_2 diffraction peaks, both in the meso-TiO_2 reference sample and in meso-TiO_2/Fe_2O_3, with anatase as a minor component. No other crystalline peaks were detected. TEM images showed distinct crystal lattice planes, with fast Fourier transforms (FFT) again identifying Fe_2O_3 and TiO_2 within the composite material. The average crystallite diameter for all crystal phases present within meso-TiO_2/Fe_2O_3 was between 12 and 14 nm, as determined using the Scherrer equation. The size distribution of the aggregated particles was disperse, with diameters of 0.5-50 μm when measured by SEM, and pH-dependent diameters of 0.4-2.4 μm when measured by DLS. The lower particle size maximum obtained by DLS may be due to poor suspension of larger particles. These results are presented in detail within the Supplementary Information.

For meso-TiO_2, Fe_2O_3 and meso-TiO_2/Fe_2O_3, N_2 adsorption-desorption isotherms showed IUPAC Type II adsorption branches with H3 hysteresis loops [58], indicating mesoporosity (Supplementary Information). The BET-specific surface area of meso-TiO_2 decreased after coupling with iron oxide to produce meso-TiO_2/Fe_2O_3 (from 110 to 100 m^2 g^{-1}), and the BJH average pore diameter increased (from 7.8 to 8.6 nm) (Table 1). This may indicate pore filling during iron oxide precipitation. The surface area of Fe_2O_3 was 103 m^2 g^{-1}. FeOOH had the largest surface area at 127 m^2 g^{-1}, a large pore diameter at 21 nm, and no significant hysteresis, suggesting less micro- and mesoporosity than the other samples [59].

STEM-EDS analysis was used to investigate the structure of the TiO_2/Fe_2O_3 composite, in both point analysis and mapping modes (Figure 1). The ratio between Fe and Ti was quantified at a number of features using point analysis, which were grouped into three categories: (a) areas where Ti was present without Fe, indicating an exposed TiO_2 surface; (b) regions which were predominantly Ti with a small amount of Fe, suggesting a thin coating of Fe on the TiO_2 surface; and (c) Fe-rich regions corresponding with bright features in the STEM image (*i.e.* high electron density), indicating Fe_2O_3 precipitates with a more particulate structure. Mesopores can be identified as dark spots (with ~10 nm diameter) in the lower right region of the STEM image [42]. STEM-EDS analysis of additional particles is presented in the Supplementary Information, and all particles showed significant mixing of Ti and Fe. The overall aggregate particles can therefore be considered as TiO_2 cores with an incomplete iron oxide coating, coupled with some larger, more particulate iron oxide surface precipitates.

3.2. Mineral composition as a function of probing depth

X-ray fluorescence spectroscopy (XRF), X-ray photoelectron spectroscopy (XPS), and low energy ion scattering (LEIS) were chosen to quantitatively determine the composition of meso-TiO_2/Fe_2O_3 (prior to adsorption of arsenic), owing to their different penetration depths. XRF has a probing depth in the order of micrometres, and therefore corresponds to bulk analysis for these meso-scale particles [28]. XPS probes the near surface, with a penetration depth of 1-10 nm, whilst LEIS is sensitive to the outermost surface (i.e. atomic-scale sensitivity) [28]. Using meso-TiO_2 and Fe_2O_3 reference samples as end-members, XRF analysis indicated that the bulk composition of the meso-TiO_2/Fe_2O_3 composite was 51.6 ±2.6% Fe_2O_3 and 48.4 ±2.4% meso-TiO_2 by mass. This is within error of the theoretical 50:50 mass ratio, based upon the quantities of reagents used. By comparing the intensity of $Fe2p^3/_2$ and $Ti2p^3/_2$ peaks with reference samples, XPS indicated a near surface composition of 58.7 ±2.6% Fe_2O_3 and 41.3 ±1.8% meso-TiO_2. In the LEIS depth profile, the intensity of Fe and Ti peaks came to a plateau with a dose of 2-4 $x10^{15}$ ions cm^{-2}, corresponding to a sputter depth of 1-2 Å (Figure 2a). This is between one and two atomic layers. LEIS analysis indicated a composition of 68.0 ±0.7% Fe_2O_3 and just 32.0 ±0.3% meso-TiO_2 at the outermost surface (Figure 2b).

These results demonstrate that the surface of meso-TiO_2/Fe_2O_3 is enriched in iron oxide relative to the bulk material (Figure 2c), agreeing with STEM-EDS analysis (Section 3.1). This iron oxide enrichment is analogous to the fine surface coatings encountered in natural sediments, which have caused previous problems in achieving accurate CA models using other characterisation techniques [9]. Since Fe_2O_3 was precipitated from solution over a solid meso-TiO_2 support, the observed iron oxide surface coating is not surprising. It is worth noting that despite being sensitive to the near surface, XPS only partially captured the total iron oxide enrichment. Since the penetration depth of XPS is on the same scale as the crystallite diameter (~12-14 nm), this suggests that much of the iron oxide surface coating is very thin (<10 nm). XRF, XPS and LEIS all provided good precision, as all uncertainties were less than 3% (calculated using Equation 2).

3.3. Investigation of component additivity in surface charge

Potentiometric titration curves for the meso-TiO_2/Fe_2O_3 composite and reference samples are presented in Figure 3a. The point of zero salt effect (pzse) was used as a measure of the point of zero charge. The pzse of all reference samples agreed with the literature, occurring at pH 4.80±0.14 for meso-TiO_2; pH 8.88±0.16 for Fe_2O_3; and pH

9.05±0.35 for FeOOH [60 61]. For meso-TiO_2/Fe_2O_3, the pzse occurred at pH 7.32±0.12. Further details are provided in the Supplementary Information.

To assess whether the surface proton excess of meso-TiO_2/Fe_2O_3 obeys component additivity, experimental observations were compared with predicted results, calculated using a linear combination of reference samples (meso-TiO_2 and Fe_2O_3, Equation 6). Three different CA predictions were calculated, where the weighting of meso-TiO_2 and Fe_2O_3 reference samples was set to each of the mass fractions determined previously: (i) in the bulk material (XRD); (ii) at the near surface (XPS); and (iii) at the outermost surface (LEIS) (Figure 3b, c, d). The accuracy of CA predictions increased in the order XRF<XPS<LEIS (Figure 4). When using the bulk mass ratio determined by XRF, the contribution of meso-TiO_2 was overestimated, predicting a low pzse at pH 6.6. XPS predicted a pzse at pH 6.8. It was only when weighting the reference samples according to LEIS analysis that the predicted pzse was within experimental error (pH 7.2 versus pH 7.32±0.12). These results demonstrate that the surface protonation of meso-TiO_2/Fe_2O_3 can be accurately modelled using the CA approach, but only when constrained to the outermost surface composition, due to the iron oxide surface coating.

3.4. Investigation of component additivity in arsenic adsorption

Adsorption isotherms were obtained to investigate whether LEIS characterisation of the outermost surface would also provide the most accurate CA prediction of arsenic adsorption onto meso-TiO_2/Fe_2O_3. Langmuir and Freundlich adsorption isotherms were used: firstly, to allow component additivity to be assessed with fewer fitting variables than the SCM, and secondly, to investigate the adsorption mechanism. The Langmuir model describes a sorbate binding to a limited number of homogeneous surface sites. Once a monolayer has been formed, the sorbent is saturated and adsorption ceases. In contrast, the Freundlich model has no upper limit to adsorption and so can fit both monolayer adsorption to a heterogeneous surface [62] and multilayer sorption [63]. Experiments were conducted at pH 7, being representative of the arsenic-contaminated groundwaters of the Bengal Basin (Bangladesh and India), with 0.01 M NaCl representing the approximate ionic strength of these groundwaters [64]. The results are presented in Figure 5 and adsorption isotherm parameters are presented in Table 1.

For As(V), differences between the goodness of fit in the Langmuir and Freundlich models were insignificant. The average coefficient of determination (R^2) of the three reference sorbents was 0.749±0.093 for the Langmuir model, and 0.757±0.235 for the Freundlich model. However, the plateau in adsorption of As(V) at high C_e values suggested that As(V) primarily binds via monolayer adsorption, as per the Langmuir model (Figure 5a-b). There was no evidence of multilayer adsorption.

In contrast, the Freundlich model gave a significantly better fit for adsorption of As(III) (R^2=0.990±0.070 versus 0.867±0.079 for Langmuir), with no adsorption plateau observed at high As(III) concentrations (Figure 5c-d). This suggests that As(III) adsorption proceeded either via monolayer adsorption onto a heterogeneous surface, or via multilayer formation. As the Langmuir model successfully fitted As(V) adsorption isotherms, suggesting that the surface of each sample was homogeneous, the Freundlich adsorption isotherm most likely indicates multilayer sorption of As(III) over all reference samples at pH 7.0±0.1 in 0.01 M NaCl. This is in agreement with multiple authors, who have identified As(III) as forming surface precipitates, or undergoing surface polymerisation, with iron oxide sorbents, starting at surface coverages between 1 and 10 μmol m^{-2} [65 66 67]. The strongest evidence for As(III) surface precipitation onto iron oxides is provided by Morin *et al.*, where a combination of high resolution transmission electron microscopy (HR-TEM) and extended X-ray absorption fine structure (EXAFS) spectroscopy was used to identify an amorphous arsenic-rich coating over Fe_3O_4 nanoparticles. This arsenic (hydr)oxide coating was observed when As(III) adsorption exceeded 2 μmol m^{-2}, and grew to a thickness of 10 nm (pH 7.2, C_e=0.15 μM to 10 mM, 0.1 M NaCl) [67]. In our work, adsorption isotherms were obtained with a maximum surface coverage of 4.9 μmol m^{-2} for Fe_2O_3 (C_e=370 μM) and 3.0 μmol m^{-2} for meso-TiO_2 (C_e=650 μM). Adsorption isotherms in the present work were therefore conducted beyond the threshold where As(III) surface precipitation has been previously identified.

Evidence of As(V) surface precipitation is less frequently observed within the literature, though it is more likely at acidic pH [68]. Mamindy-Pajany *et al.* observed surface precipitation behaviour for adsorption of As(V) onto Fe_2O_3 (starting at q_e >3 μmol m^{-2}, C_e >100 μM, pH 6, 0.01 M $NaNO_3$) but not for FeOOH (with data obtained up to q_e=1.4 μmol m^{-2} and C_e=150 μM) [69]. In contrast, the adsorption isotherms reported by Jeong *et al.* show As(V) surface precipitation behaviour over Al_2O_3 (when q_e >2.4 μmol m^{-2}, C_e >53 μM, pH 5-9, no specific electrolyte) but not for Fe_2O_3 (with data up to q_e=1.6 μmol m^{-2} only, C_e=6.7 μM) [70]. Jia *et al.* identified formation of As(V) surface precipitates over iron hydroxides at acidic pH, but not at pH 8 [68]. This precipitate was identified as "amorphous" ferric arsenate ($AsFeO_4$) or scorodite ($FeAsO_4 \cdot 2H_2O$) using XRD [68]. There was no evidence for multilayer adsorption of As(V) in our work, with adsorption isotherms reaching a definite plateau. At pH 7.0 ±0.1 As(V) is deprotonated, and the repulsive negative charge between these oxyanions may explain why surface

precipitation is less likely than for As(III). As well as pH differences, reaction kinetics may also explain the inconsistent observations in the literature, since surface precipitation is significantly slower than monolayer surface adsorption [71]. Bulk precipitation of As(V) and As(III) was observed neither in control experiments, nor in PHREEQC modelling (Supplementary Information).

Component additive predictions for adsorption of arsenic onto meso-TiO_2/Fe_2O_3 were calculated as a linear combination of meso-TiO_2 and Fe_2O_3 adsorption isotherms, weighted according to material composition at the bulk, near surface and outermost surface (using Equation 6). As with surface charge, the most accurate CA predictions of As(V) adsorption were achieved when using the outermost surface (LEIS analysis) to weight each component within the model (Figure 5a, b). R^2 values were 0.786, 0.826 and 0.861 for the XRF-, XPS- and LEIS-weighted linear combinations, respectively.

Unlike monolayer surface protonation and As(V) adsorption, multilayer As(III) adsorption failed to provide the most accurate CA prediction when LEIS was used to weight each component. The LEIS-weighted CA prediction overestimated experimental results (Figure 5c, d), with R^2 values of 0.975, 0.968 and 0.956 for XRF-, XPS- and LEIS-weighted linear combinations of As(III) adsorption isotherms, respectively. Unlike monolayer adsorption, multilayer processes are influenced by sorbent morphology, e.g. pore size and surface roughness [72] [73] [74]. The inaccuracy of LEIS can therefore be explained by differences between the surface morphology of reference samples and the composite meso-TiO_2/Fe_2O_3 (Table 1). This is discussed further in section 3.6.

Improvements in the accuracy of CA predictions using LEIS, for both surface charge and As(V) adsorption, highlight the importance of using surface-sensitive characterisation techniques to best constrain the contribution of each solid phase to the overall composite surface. Our results suggest that inappropriate component weighting will have limited the success of many previous CA models, e.g. studies using mass ratios of the bulk material will have failed to identify the surface enrichment of certain components.

3.5. Determination of equilibrium constants for the surface complexation model

Component additive SCMs describe the composite sorbent as a combination of surface components, and each surface component has its own adsorption equilibrium constants [9]. In this work, equilibrium constants were obtained experimentally for the surface reactions of each meso-TiO_2/Fe_2O_3 surface component, by fitting data collected using the single-component reference sorbents. In this work, each surface component was modelled using a SCM variant known as the extended triple layer model (ETLM) [49].

Estimates of the surface site density were taken from the literature [41] [50], and equilibrium constants for surface hydroxyl (de)protonation were predicted using Sverjensky's empirical formula [48]. The inner capacitance (C_1) of each reference sample, and equilibrium constants for electrolyte adsorption were determined by optimising potentiometric titration data with FITEQL (Supplementary Information). Surface charge titration curves were best modelled with C_1 set to 0.9 F m^{-2} for FeOOH and 0.8 F m^{-2} for Fe_2O_3. This is close to the 1.0 F m^{-2} determined by Kanematsu *et al.* (FeOOH in 0.01 to 0.1 M $NaNO_3$) [41], and the 0.9 F m^{-2} predicted by Sverjensky (Fe_2O_3 in NaCl) [51]. Using the 0.01 M NaCl titration, meso-TiO_2 was fit best with 1.3 F m^{-2}. This agrees with the 1.31 F m^{-2} for TiO_2 (in 0.01 M NaCl) determined by Sverjensky *et al.* [75], and 1.2 F m^{-2} for rutile TiO_2 (in 0.01-0.1 M NaCl) determined by Jonsson *et al.* [52].

Equilibrium constants for the surface complexation of arsenic were determined by fitting the ETLM to experimental pH adsorption edges. The optimised SCM gave a good fit for the adsorption of As(V) onto FeOOH (Figure 6a). As(V) adsorption was greatest at acidic pH, owing both to the electrostatic attraction between positive mineral surface and negative As(V) oxyanion, and to the availability of protons needed to form bidentate $(>SO)_2AsO_2H$ and $(>SO)_2AsO_2^-$ surface complexes from aqueous $H_2AsO_4^-$ and $HAsO_4^{2-}$. Results were similar for Fe_2O_3, with a good fit above pH 4 (Figure 6b). Between pH 3 and 4, the high removal of As(V) by Fe_2O_3 (up to 99%) was not matched by the ETLM. This may be due to As(V) surface precipitation at acidic pH, as discussed in section 3.4. Compared with FeOOH, the $(>SO)_2AsO_2H$ and $>SOAsO_3^{2-}$ surface complexes were more and less significant, respectively, when fitting the pH adsorption edge of Fe_2O_3. For meso-TiO_2, experimental data was successfully modelled without the protonated $(>SO)_2AsO_2H$ complex. This complex was therefore ommitted in order to reduce the number of fitted parameters. At pH 7, the proportion of adsorbed As(V) present as negative species increased in the order Fe_3O_4<FeOOH<meso-TiO_2. This matches the order of increasing inner-capacitance, C_1. With the highest capacitance, meso-TiO_2 best accommodates the negative charge of $(>SO)_2AsO_2^-$ and $>SOAsO_3^{2-}$.

The optimised ETLM provided a good fit for the adsorption of As(III) onto FeOOH, with $(>SO)_2AsO^-$ as the major complex (Figure 6d). In contrast, the $(>SO)_2AsO^-$ complex was less important for Fe_2O_3 than the $(>SO)_2AsOH$ and $>SOH_2^+$---$AsO(OH)_2^-$ complexes (Figure 6e). Again, this correlates with the higher capacitance of FeOOH, which better accommodates negatively charged surface complexes. The hydrogen-bonded $>SOH_2^+$--

-$AsO(OH)_2^-$ complex was most prevalent for meso-TiO_2, where innersphere $(>SO)_2AsO^-$ only dominated below pH 7 (Figure 6f). A good experimental fit could not be achieved when substituting the hydrogen-bonded complex for monodentate $>SOAsO_2^-$. As with As(V), meso-TiO_2 did not require a protonated bidentate complex (*i.e.* $(>SO)_2AsOH$) to achieve the best possible fit for the As(III) adsorption edge, and this complex was therefore omitted.

All SCM parameters are presented in Table 2.

3.6. Modelling multilayer arsenic(III) adsorption

The SCM parameters obtained using pH adsorption edges were validated by predicting adsorption isotherms and comparing the results against experimental observations. The model successfully predicted the experimental As(V) adsorption isotherms for all single-component reference samples (FeOOH, Fe_2O_3 and meso-TiO_2, Supplementary Information). In contrast, the extent of As(III) adsorption was significantly underestimated for all reference samples: the SCM approximated the form of the Langmuir adsorption isotherm with a definite plateau, failing to capture the observed Freundlich behaviour (Supplementary Information, Figure S22). The difference between model and experimental observations is attributed to multilayer As(III) adsorption, and demonstrates a limitation in using surface complexation reactions determined from pH adsorption edges. SCMs are typically limited mechanistically to monolayer adsorption (there is no more than one surface complex per surface site, and adsorption ceases once all sites are occupied). However, several studies have identified As(III) surface precipitation on minerals including Fe_2O_3, as discussed in section 3.4 [67] [65] [66]. This discrepancy between experimental data and the ETLM prediction of As(III) adsorption at high concentrations is observed in other data sets such as Sverjensky and Fukushi, 2006 (see figures 3b, 4b and 5c in their paper) [66]. Accurate CA-SCMs require accurate single-component reference SCMs, and therefore, multilayer adsorption of As(III) was introduced into our model (Equation 17).

Farley *et al.* and Lützenkirchen and Behra previously developed surface precipitation models to account for the experimentally observed adsorption of metal cations onto metal (hydr)oxide surfaces. These models sucessfully approximated the observed Freundlich and BET isotherms, rather than the Langmuir isotherm [76] [71]. In the surface precipitation model, formation of each surface complex generates a new surface site for further sorbate binding. These previous studies considered the mineral surface as a solid solution. As adsorption progresses, the surface transitions from pure sorbent towards a bulk sorbate precipitate. In the solid solution model, precipitation and dissolution reactions of both sorbate and sorbent surface are included, and the activity of each component within the solid solution is a function of its mass fraction.

Sorbent dissolution was considered unlikely in this work. Previous studies have shown that: at pH 3, suspensions of 40 m^2 L^{-1} TiO_2 release <10 nM titanium into solution [77]; at pH 5, suspensions of 10 g L^{-1} FeOOH release <1 nM iron per hour [78]; at pH 2.4, after 20 hours, suspensions of 5 g L^{-1} Fe_2O_3 release <3 µM iron [79]. These concentrations are all far lower than the 100-600 µM As(III) used in this work and were all observed at acidic pH (whereas pH 7 was used in this work). Therefore, rather than modelling the system as a solid solution (*i.e.* including sorbent dissolution reactions), multilayer sorption was modelled using the simpler Equation 17. This reaction was added to the SCM, and a surface precipitation equilibrium constant was obtained for each single-component reference sorbent by fitting the experimental adsorption isotherm, accounting for the difference between the total extent of As(III) adsorption observed experimentally, and the smaller quantity predicted by the monolayer-only SCM. Including this surface precpitation reaction allowed the experimental adsorption isotherms of all three reference samples to be successfully reproduced (Supplementary Information).

The optimised equilibrium constants for surface precipitation increased in the order FeOOH<Fe_2O_3<meso-TiO_2 (Table 2), which corresponds to the steepness observed in the Freundlich isotherm of each sorbent. This also correlates with surface morphology, as pore sizes decreased in the order FeOOH>Fe_2O_3>meso-TiO_2 (21, 9 and 8 nm respectively). Smaller pores provide increasingly concaved surfaces with smaller contact angles, promoting adsorption and surface precipitation [72]. This suggests that the surface precipitation equilibrium constants may be conditional, depending upon the morphology of each sample.

We have not directly identified surface precipitation in this work (e.g. spectroscopically), and the principal purpose of modelling surface precipitation was to provide single-component SCMs that reproduce the experimental adsorption isotherms, in order to develop the final CA-SCM. In line with Morin *et al.*, who identified an amorphous As(III) mineral surface precipitate formed on Fe_3O_4, we have provisionally labelled this surface precipitate as "As_2O_3" [67].

3.7. Accuracy of the component additive surface complexation model, constrained using low energy ion scattering

To assess the accuracy of the CA-SCM, meso-TiO_2/Fe_2O_3 adsorption isotherms were modelled and compared against experimental observations. In the CA-SCM, the total surface area of meso-TiO_2/Fe_2O_3 (100 m^2 g^{-1}) was divided between meso-TiO_2 and Fe_2O_3, according to the mass ratios calculated using XRF, XPS, and LEIS analysis. The SCM parameters used to model meso-TiO_2/Fe_2O_3 (site density, capacitance and all equilibrium constants) were all experimentally determined using the single-component reference sorbents (i.e. the CA-SCM uses the parameters determined in sections 3.5 and 3.6, and presented in Table 2). The density of surface sites was maintained as 3.0 sites nm^{-2} for meso-TiO_2 and 4.0 sites nm^{-2} for Fe_2O_3, *i.e.* assuming that the concentration of surface hydroxyls per unit area in the reference samples and the composite sorbent is equivalent. The CA-SCM was modelled using separate electrical double layers for meso-TiO_2 and Fe_2O_3 surface components, as overlap is not considered to be significant [10]. For completeness, a comparison of results obtained using discrete and shared electrical double layers is given in the Supplementary Information.

The adsorption isotherms predicted by the final CA-SCM are presented in Figure 7, with the goodness of fit, and errors between experimental and calculated results presented in Table 3. The accuracy of the CA-SCM towards modelling As(V) adsorption improved with surface-sensitive component weighting, in the order XRF<XPS<LEIS (Figure 7a). In the LEIS-weighted CA-SCM, the root-mean-square error (RMSE) was 0.12 µmol m^{-2}, or 8.3%. As(V) adsorption was overestimated when C_e<60 µM, and overestimated when C_e>60 µM. When compared with XRF (representing the bulk mass ratios used in most previous CA-SCM studies), using LEIS to weight the CA-SCM reduced the average absolute error by 82%, the average relative error by 96%, and the RMSE by 42%. These results indicate that CA-SCM accuracy is improved when components are weighted acording to surface-sensitive analysis (ideally the outermost surface, *i.e.* using LEIS). The speciation and partitioning of adsorbed As(V) in the CA-SCM is presented in Figure 7b.

Much like the linear combination of Freundich adsorption isotherms, LEIS-weighting failed to provide the most accurate CA-SCM for As(III) adsorption, systematically overestimating the experimental results (Figure 7c). Consequently, the accuracy of the CA-SCM decreased when using LEIS, instead of XRF, to weight components (Table 3). Section 3.6 discussed how the equilibrium constant for the As(III) surface precipitation reaction is correlated with sorbent morphology: larger pore sizes result in smaller equilibrium constants. Some of the porosity of meso-TiO_2 is lost in the composite material, due to pore filling by Fe_2O_3 (section 2.1). This implies that the equilibrium constants obtained for the adsorption of As(III) onto the reference samples are too large for the composite system, resulting in the positive error that is observed in the CA-SCM predictions. This is an important finding, as it suggests that when the morphology and porosity of composite and reference samples are different, CA models are likely to fail in their description of multilayer adsorption processes.

4. Conclusions

We developed a component additive (CA) model for the adsorption of arsenic onto a composite sorbent, using parameters obtained from single-component reference sorbents. The key finding is that CA models are best constrained when surface-sensitive analytical techniques are used to quantify the sorbent composition: In this work, the LEIS-weighted CA model predicted monolayer As(V) adsorption and surface acidity most accurately. CA models should not be weighted according to the mass ratio of the bulk material: In this work, bulk analysis (using XRF) failed to identify a fine iron oxide surface coating, resulting in significant inaccuracies. Near surface analysis using XPS provides better constraints than the mass ratio of the bulk material. The CA-SCM overstimated multilayer As(III) adsorption, since the morphologies of the composite sorbent and reference samples were different.

Surface-sensitive analytical techniques offer a number of improvements over previous approaches to CA-SCM weighting. Firstly, unlike mass ratios, the significance of fine precipitates and surface coatings is captured [9 10 24]. Secondly, unlike chemical extraction, the technique is precise, and the probing depth is known [9 24]. Thirdly, LEIS and XPS can quantify ternary sorbent surfaces, which cannot be characterised using adsorption isotherms alone [25]. Future work should use surface-sensitive analytical techniques to develop increasingly accurate component additive models. These models should be used to (a) investigate the adsorption mechanisms of composite sorbents, and (b) engineer high performing multifunctional sorbents.

5. Acknowledgements

Funding: This work was supported by the Engineering and Physical Sciences Research Council (EPSRC) [grant number EP/N509486/1] and the EPSRC Centre for Doctoral Training in the Advanced Characterisation of Materials (CDT ACM). A. K. thanks Imperial College for a Junior Research Fellowship, the EPSRC for a Capital

Award Emphasising Support for Early Career Researchers and the Royal Society for an Equipment Grant (RSG\R1\180434).

6. Tables

Sample	FeOOH	Fe_2O_3	Meso-TiO_2	Meso-TiO_2/Fe_2O_3
BET-specific surface area (m^2 g^{-1})	127	103	110	100
BJH-specific average pore diameter (nm)	21.2	8.9	7.8	8.6
Langmuir adsorption isotherm parameters for As(V)				
K_L (μM^{-1})	0.961 ±0.232	0.126 ±0.030	0.0536 ±0.009	0.070 ±0.015
Q_{max} (μmol m^{-2})	1.97 ±0.08	2.08 ±0.07	1.21 ±0.04	1.81 ±0.05
R^2 (linear form)	1.000	0.999	0.999	0.991
R^2 (C_e vs q_e)	0.623	0.763	0.849	0.654
Q_{max} (mg g^{-1})	18.7 ±0.8	16.1 ±0.5	9.62 ±0.3	13.6 ±0.4
Freundlich adsorption isotherm parameters for As(III)				
n	5.71 ±0.28	4.26 ±0.26	3.61 ±0.19	3.51 ±0.11
K_F (μmol m^{-2} $\mu M^{-1/n}$)	1.11 ±0.08	1.19 ±0.08	0.49 ±0.04	0.69 ±0.03
R^2 (linear form)	0.975	0.988	0.977	0.994
R^2 (C_e vs q_e)	0.907	0.979	0.992	0.996

Table 1: Adsorption isotherm parameters (Langmuir model for As(V) adsorption and Freundlich model for As(III) adsorption). Adsorption isotherm parameters were calculated using C_e in μM and Q_e and Q_{max} in μmol mol^{-2} for easier comparison with literature sorbents differing in surface area. Adsorption isotherm parameters were calculated using 7-12 experimental data points, and uncertainties (expressed as one standard deviation, or 1σ) were determined using the nonlinear regression Monte Carlo method described by Hu et al. [80].

Aqueous phase reactions *			
log β	$+H^+$	$+2H^+$	$+3H^+$
AsO_4^{3-}	11.60	18.35	20.60
AsO_3^{3-}	13.41	25.52	34.74

Surface reactions				
	Material	FeOOH	Fe_2O_3	meso-TiO_2
Physical properties	BET-specific surface area (m^2 g^{-1})	127	103	110
	Site density (sites nm^{-2})	4.0	4.0	3.0
Capacitance	C_1 (F m^{-2})	0.9	0.8	1.3
	C_2 (F m^{-2})	0.2	0.2	0.2
Surface charge and electrolyte adsorption	$logK_1$	5.59 (6.3)	5.48 (6.09)	1.13 (1.65)
	$logK_2$	-12.6 (11.9)	-12.3 (11.7)	-8.47 (7.95)
	$logK_M$	-8.79 ±0.24 (3.82)	-8.81 ±0.08 (3.50)	-4.88 ±0.19 (3.59)
	$logK_L$	9.10 ±0.19 (3.51)	8.51 ±0.05 (3.02)	4.37 ±0.32 (3.24)
As(V) surface complexation	$logK_{(>SO)_2AsO_2^-}$	11.9 (2.71)	10.3 (1.33)	11.0 (10.74)
	$logK_{(>SO)_2AsO_2H}$	11.8 (2.61)	11.8 (2.83)	-
	$logK_{>SOAsO_3^{2-}}$	6.12 (0.53)	2.20 (-3.29)	5.00 (3.87)
As(III) surface complexation	$logK_{(>SO)_2AsO^-}$	4.67 (-4.52)	2.41 (-6.56)	6.20 (5.94)
	$logK_{(>SO)_2AsOH}$	7.93 (-1.26)	8.40 (-0.57)	-
	$logK_{>SOH_2^+---AsO(OH)_2^-}$	5.49 (-0.104)	5.44 (-0.045)	3.75 (2.62)
As(III) surface precipitation	$logK_{ppt}$	2.28	3.05	3.32

Table 2: Surface complexation modelling parameters for the ETLM. All surface complexation constants are presented in the hypothetical 1.0 M standard state ($logK^0$) used in FITEQL, and equilibrium constants for the site-occupancy standard state ($logK^0$) are presented in parentheses.

**aqueous speciation constants are taken from Dixit and Hering [54], in turn from Schecher and McAvoy [55]. Electrolyte adsorption constants were calculated from the average of 3 titrations, arsenic surface complexation constants were calculated from pH adsorption edges with 14 or 15 experimental data points each, and As(III) surface precipitation constants were calculated from adsorption isotherms with 11 to 17 data points. Uncertainties in $logK_M$ and $logK_L$ were calculated as the standard deviation between three potentiometric titrations at different ionic strengths. Values of FITEQL's error function, V_y, were calculated when fitting the SCM to experimental data, and are presented and discussed in the Supplementary Information.*

Table 3: Accuracy of the CA-SCM with components weighted by XRF (bulk), XPS (near surface) and LEIS (outermost surface) analysis. Errors represent the difference between the adsorption isotherms predicted by each model and the experimental data points. The root mean square error (RMSE) was calculated using the formula $RMSE = \sqrt{\sum_{i=1}^{n} \frac{(y_i - \hat{y}_i)^2}{n}}$, *where y_i is the experimental observation, $\hat{y}$ is the predicted result, n is the number of data points (8 for As(V) and 10 for As(III)), and i is the unique index assigned to each data point.*

Sorbate	Property	XRF	XPS	LEIS	% change in error (LEIS-weighting vs. XRF)
As(V)	R^2	0.6706	0.8005	0.8886	-
	average absolute error (μmol m^{-2})	-0.16 ±0.13	-0.10 ±0.13	-0.029 ±0.12	-82
	average relative error (%)	-9.4 ±7.5	-5.5 ±8.1	-0.4 ±8.9	-96
	RMSE (μmol m^{-2})	0.20	0.16	0.12	-42
	RMSE (%)	12	9.3	8.3	-29
As(III)	R^2	0.9767	0.9553	0.9013	-
	average absolute error (μmol m^{-2})	0.11 ±0.16	0.22 ±0.14	0.37 ±0.12	230
	average relative error (%)	7.9 ±11	13 ±11	20 ±12	150
	RMSE (μmol m^{-2})	0.19	0.26	0.38	106
	RMSE (%)	13	17	23	79

7. Figures

(a)

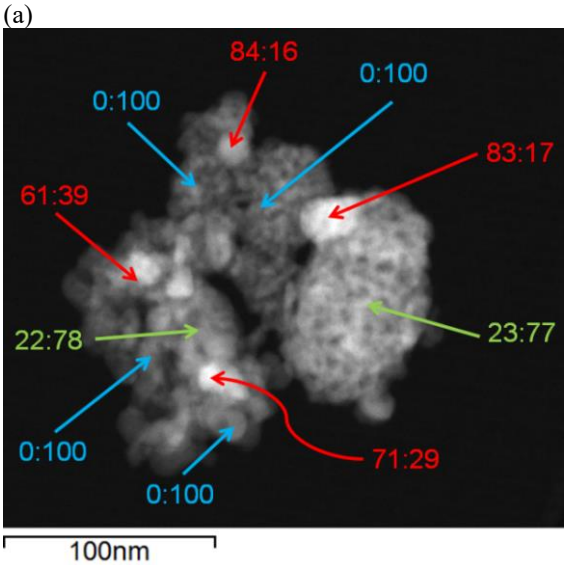

(b)

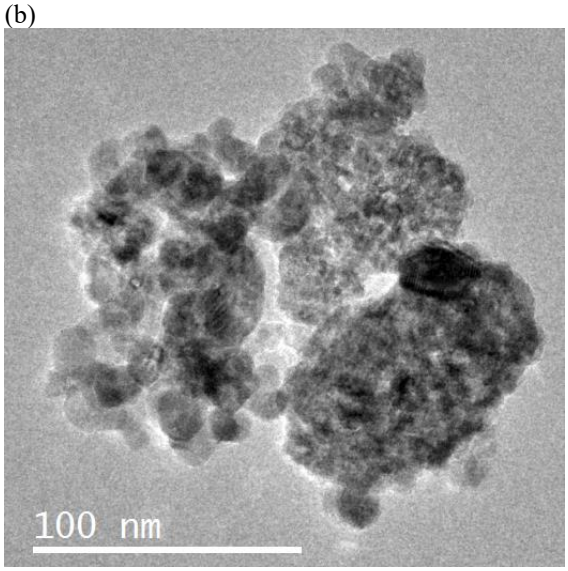

(c)

(d)

ISSN: 2283-7175 | https://tbfpeerjournal.org/

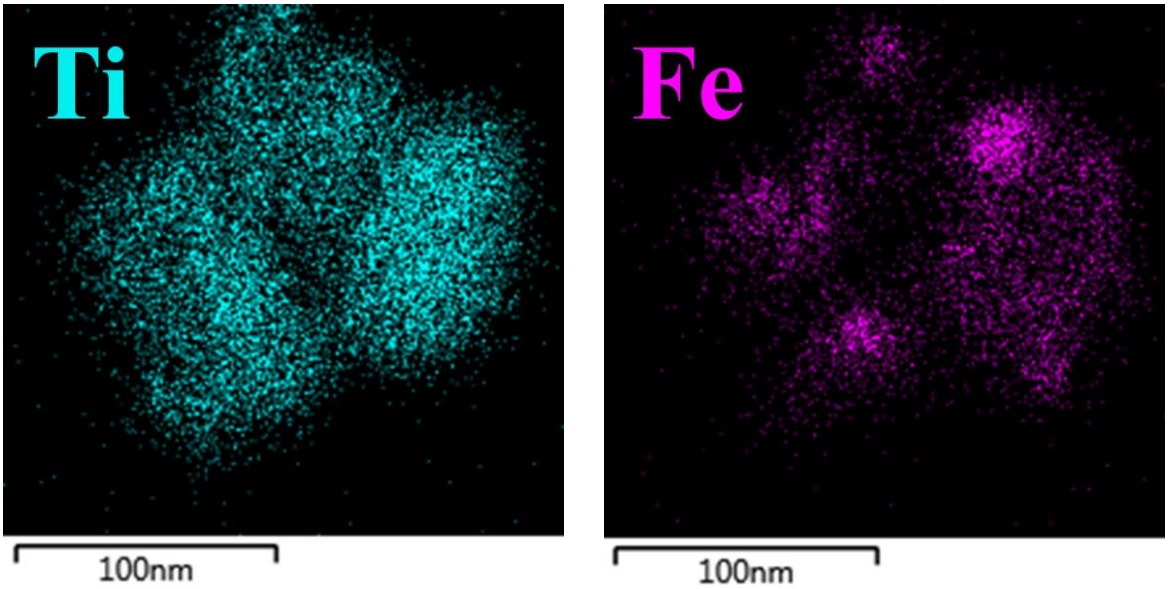

Figure 1: STEM-EDS analysis of meso-TiO_2/Fe_2O_3. (a) STEM image with Fe:Ti ratios determined by STEM-EDS point analysis. Red labels denote Fe-majority regions, green labels denote Ti-majority regions and blue labels denote Ti-only regions. (b) TEM image of the same particle. STEM-EDS mapping of (c) Ti and (d) Fe. STEM-EDS analysis of further particles is provided in the Supplementary Information.

THEORETICAL BIOLOGY FORUM
ISSN: 2283-7175 | https://tbfpeerjournal.org/

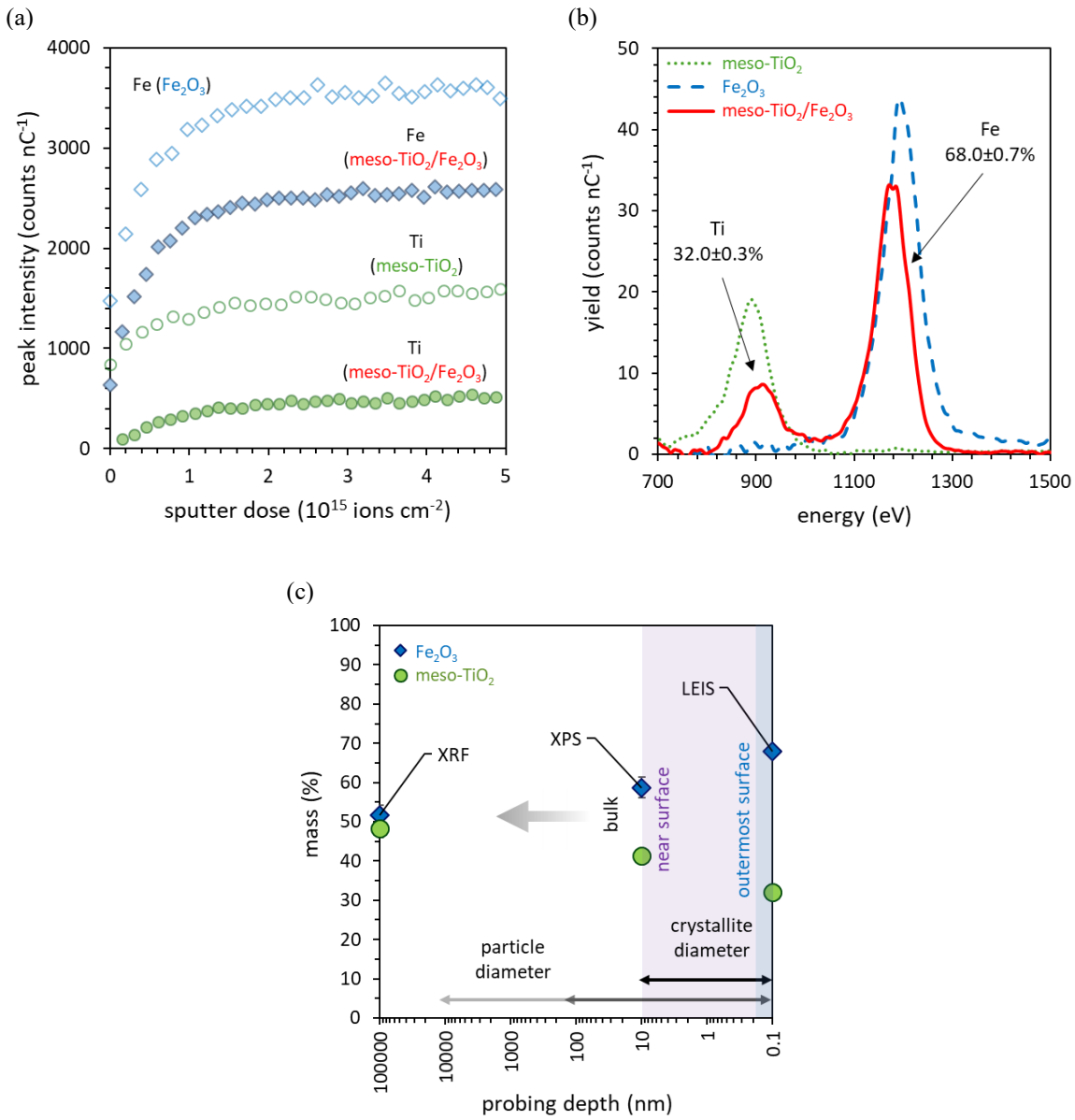

Figure 2: Mineral composition as a function of probing depth: (a) The LEIS depth profile of meso-TiO_2/Fe_2O_3 and reference samples. (b) LEIS determination of the outermost surface composition using the areas of the Fe and Ti peaks. (c) A comparison of the composition of meso-TiO_2/Fe_2O_3 in the bulk material, and at the near and outermost surfaces, using XRF, XPS and LEIS analysis respectively.

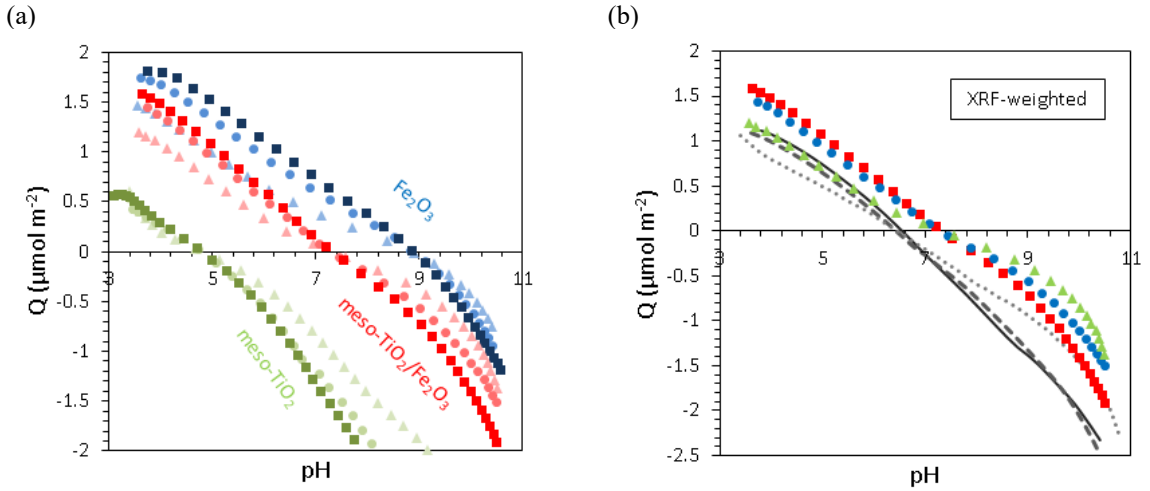

ISSN: 2283-7175 | https://tbfpeerjournal.org/

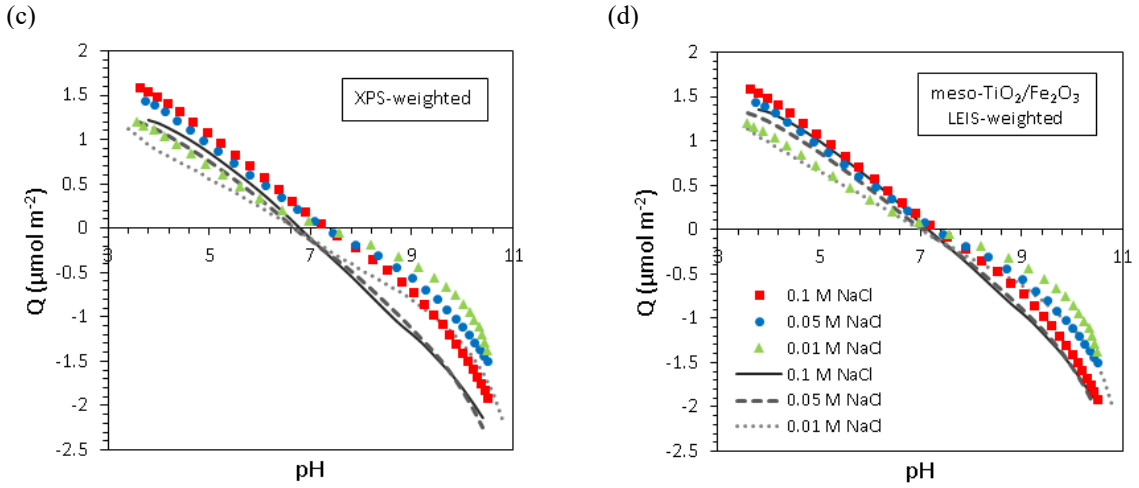

Figure 3: Component additivity in surface charge, determined by potentiometric titration. (a) A comparison of meso-TiO_2/Fe_2O_3 and single-component reference samples. The surface charge of meso-TiO_2/Fe_2O_3 was predicted using a linear combination of single-component reference samples, weighted according to (b) the bulk composition (XRF analysis), (c) the near-surface composition (XPS analysis), and (d) the outermost surface composition (LEIS analysis). Titrations were carried out in 0.1 M NaCl (squares), 0.05 M NaCl (circles) and 0.01 M NaCl (triangles). All experiments were conducted with 10 g L^{-1} sorbent. All titrations shown are forwards titrations using 0.1 M NaOH.

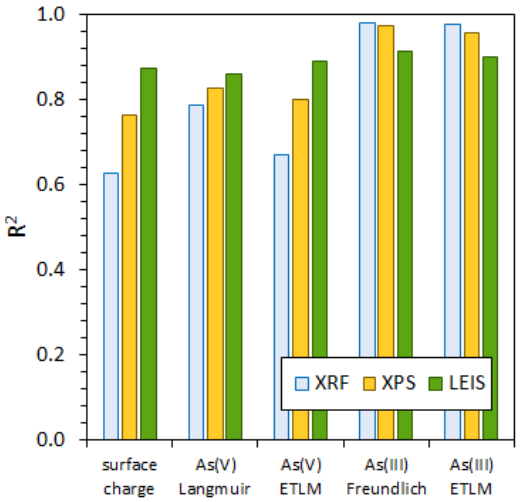

Figure 4: The goodness of fit between the component additive predictions of meso-TiO_2/Fe_2O_3 surface processes and experimental observations. R^2 indicates the coefficient of determination. Component additive predictions weighted according to XRF, XPS and LEIS analysis are compared. Values of R^2 were calculated for surface charge (potentiometric titrations), As(V) adsorption isotherms (modelled with both the Langmuir adsorption isotherm and the CA-SCM), and As(III) adsorption isotherms (modelled with both the Freundlich adsorption isotherm and the CA-SCM).

ISSN: 2283-7175 | https://tbfpeerjournal.org/

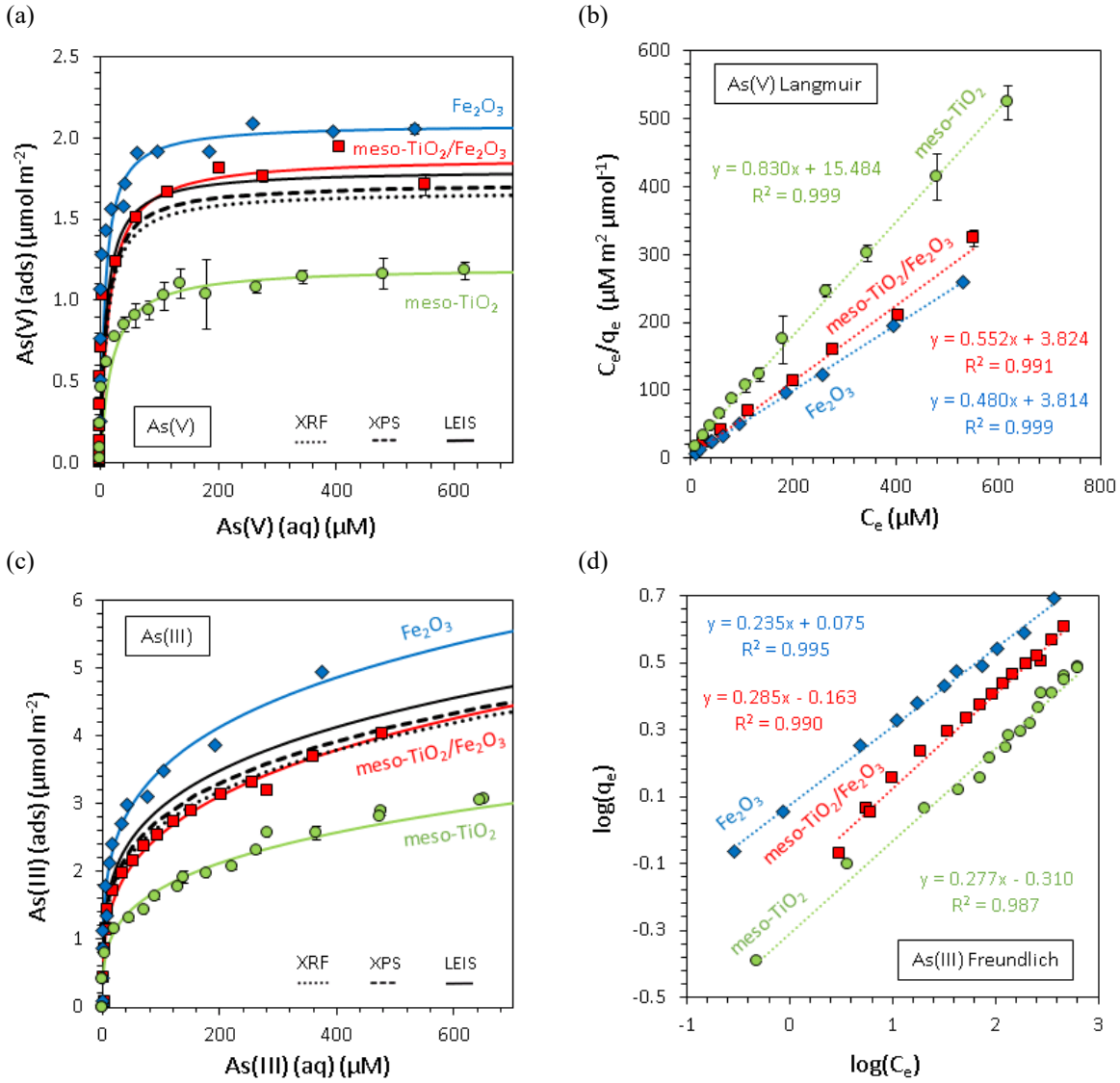

Figure 5: Component additivity in adsorption isotherms, with meso-TiO_2/Fe_2O_3 (red squares), meso-TiO_2 (green circles) and Fe_2O_3 (blue diamonds). Solid coloured lines indicate the results of adsorption isotherm fitting, whilst component additive predictions are shown using LEIS- (black solid lines), XPS- (dashed lines) and XRF- (dotted lines) weighted linear combinations of the single-component reference samples. (a) and (b) show the Langmuir fit for As(V) adsorption, whilst (c) and (d) show the Freundlich fit for As(III) adsorption. All experiments were conducted in 0.01 M NaCl, with 1 g L^{-1} sorbent, and pH 7.0 ±0.1. The average absolute uncertainty in C_e was 2.5±4.4 μM, and the average relative uncertainty was 5.2±7.8%. The average absolute uncertainty in q_e was 0.022±0.040 μmol m^{-2}, and the average relative uncertainty was 1.3±2.6%.

ISSN: 2283-7175 | https://tbfpeerjournal.org/

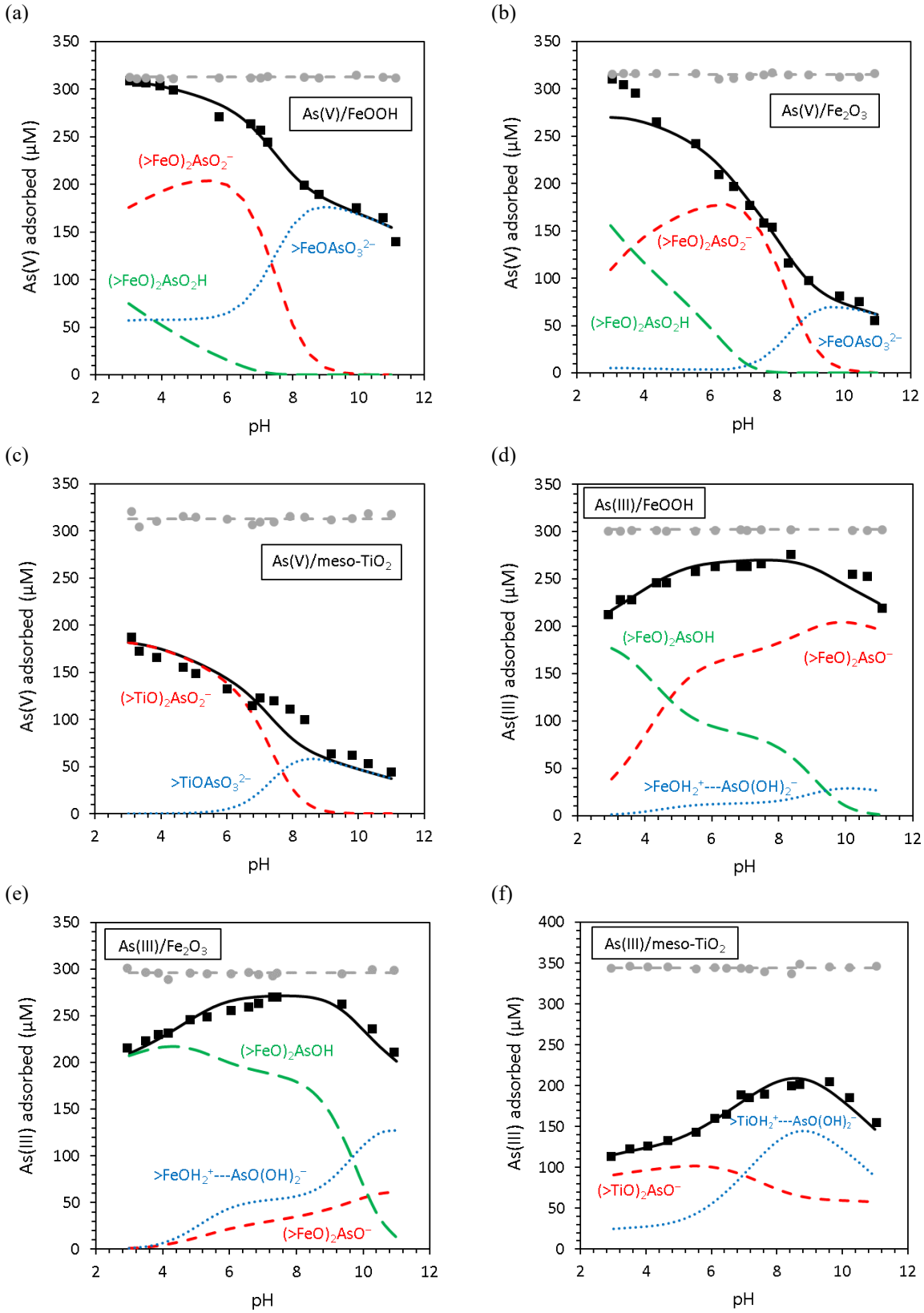

Figure 6: Determination of arsenic surface complexation constants using pH adsorption edges for As(V) (a, b and c) and As(III) (d, e and f). Experimental data is presented as total As (grey circles) and adsorbed As (black squares). The model is presented as both total adsorbed As (black solid lines), and individual surface complexes, which are presented as bidentate protonated species (green long dashed lines), bidentate deprotonated species (red short dashed lines) and monodentate species (blue dotted lines).The total concentration of As in the model is presented as the grey dashed line.Conditions were 0.01 M NaCl and 1 g L^{-1} sorbent. pH was measured to two decimal places. The average absolute uncertainty in the concentration of adsorbed As(III) was 1.8±5.8 µM, and the average relative uncertainty was 2.4±4.1%.

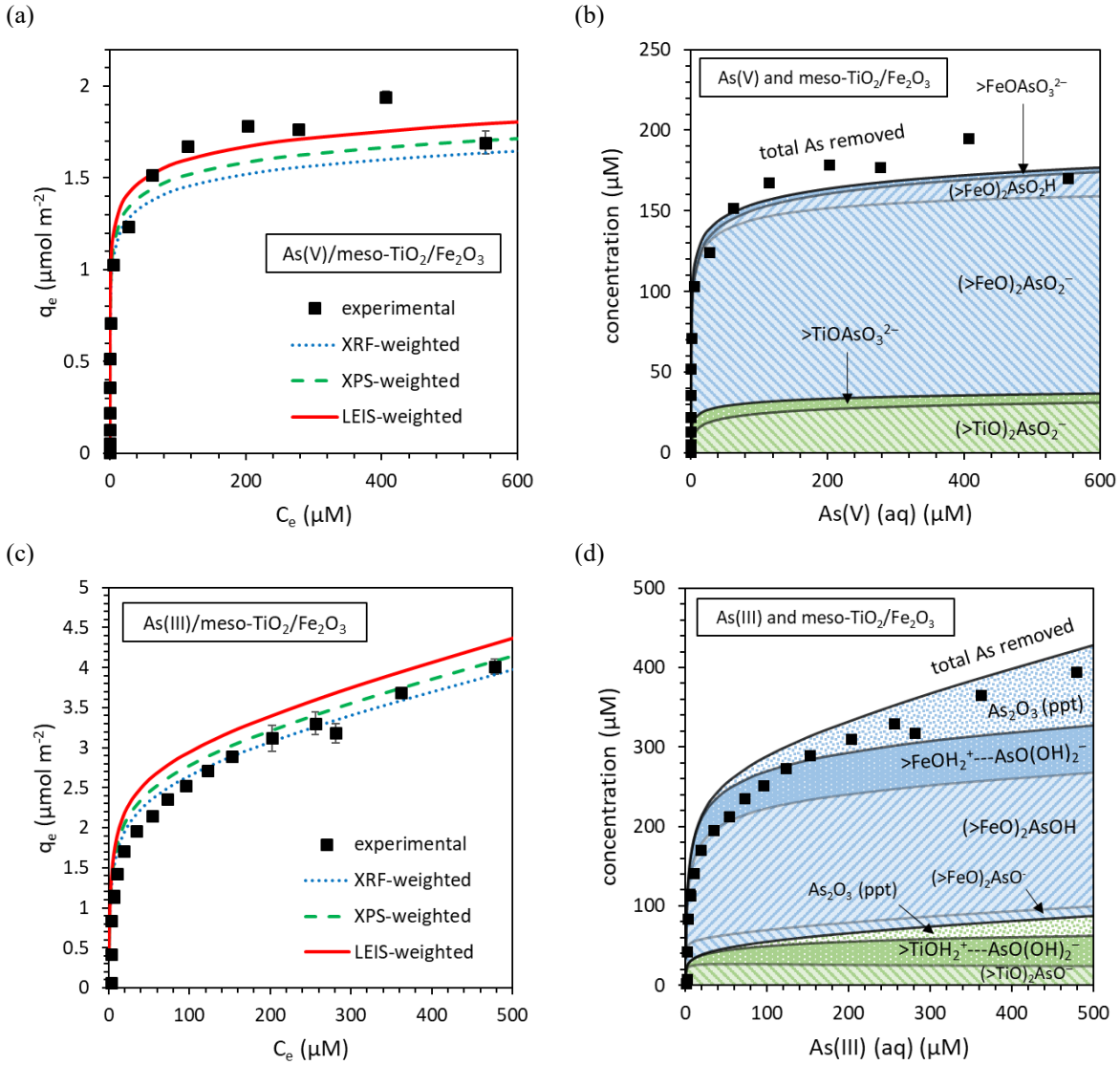

Figure 7: A comparison of adsorption isotherms predicted by the component additive surface complexation model (CA-SCM) and the experimental results. (a) As(V) adsorption predicted by the XRF-, XPS- and LEIS-weighted models, and (b) the partitioning and speciation of adsorbed As(V). (c) As(III) adsorption predicted by the XRF-, XPS- and LEIS-weighted models, and (d) the partitioning and speciation of adsorbed As(III). Conditions were 0.01 M NaCl, 1 g L^{-1} sorbent and pH 7.0 ±0.1.

8. References

(1) Bolisetty, S.; Peydayesh, M.; Mezzenga, R. Sustainable Technologies for Water Purification from Heavy Metals: Review and Analysis. *Chem. Soc. Rev.* **2019**, *48* (2), 463–487. https://doi.org/10.1039/c8cs00493e.

(2) Zemskova, L. A.; Voit, A. V.; Barinov, N. N.; Nikolenko, Y. M.; Shlyk, D. K. Composite Sorbents Based on Synthetic Manganese Oxide and Carbon Fiber. *Russ. J. Inorg. Chem.* **2016**, *61* (12), 1567–1572. https://doi.org/10.1134/S0036023616120226.

(3) Yu, L.; Peng, X.; Ni, F.; Li, J.; Wang, D.; Luan, Z. Arsenite Removal from Aqueous Solutions by γ-Fe2O3-TiO2 Magnetic Nanoparticles through Simultaneous Photocatalytic Oxidation and Adsorption. *J. Hazard. Mater.* **2013**, *246–247*, 10–17. https://doi.org/10.1016/j.jhazmat.2012.12.007.

(4) Deng, L.; Shi, Z.; Peng, X. Adsorption of Cr(VI) onto a Magnetic CoFe2O4/MgAl-LDH Composite and Mechanism Study. *RSC Adv.* **2015**, *5* (61), 49791–49801. https://doi.org/10.1039/c5ra06178d.

(5) Zhou, W.; Fu, H.; Pan, K.; Tian, C.; Qu, Y.; Lu, P.; Sun, C. Mesoporous TiO2/α-Fe2O3: Bifunctional Composites for Effective Elimination of Arsenite Contamination through Simultaneous Photocatalytic Oxidation and Adsorption. *J Phys Chem* **2008**, *112*, 19584–19589. https://doi.org/10.1021/jp806594m.

(6) D'Arcy, M.; Weiss, D.; Bluck, M.; Vilar, R. Adsorption Kinetics, Capacity and Mechanism of Arsenate and Phosphate on a Bifunctional TiO2-Fe2O3 Bi-Composite. *J. Colloid Interface Sci.* **2011**, *364* (1), 205–212. https://doi.org/10.1016/j.jcis.2011.08.023.

(7) Yahya, N.; Aziz, F.; Jamaludin, N. A.; A. Mutalib, M.; Ismail, A. F.; W. Salleh, W. N.; Jaafar, J.; Yusof, N.; A. Ludin, N. A Review of Integrated Photocatalyst Adsorbents for Wastewater Treatment. *J. Environ. Chem. Eng.* **2018**, *6* (6), 7411–7425. https://doi.org/10.1016/j.jece.2018.06.051.

(8) Jeppu, G. P.; Clement, T. P. A Modified Langmuir-Freundlich Isotherm Model for Simulating PH-Dependent Adsorption Effects. *J. Contam. Hydrol.* **2012**, *129–130*, 46–53. https://doi.org/10.1016/j.jconhyd.2011.12.001.

(9) Davis, J. A.; Coston, J. A.; Kent, D. B.; Fuller, C. C. Application of the Surface Complexation Concept to Complex Mineral Assemblages. *Environ. Sci. Technol.* **1998**, *32*, 2820–2828. https://doi.org/https://doi.org/10.1021/es980312q.

(10) Davis, J. A.; Meece, D. E.; Kohler, M.; Curtis, G. P. Approaches to Surface Complexation Modeling of Uranium(VI) Adsorption on Aquifer Sediments. *Geochim. Cosmochim. Acta* **2004**, *68* (18), 3621–3641. https://doi.org/10.1016/j.gca.2004.03.003.

(11) Ding, C.; Cheng, W.; Jin, Z.; Sun, Y. Plasma Synthesis of β-Cyclodextrin/Al(OH)3 Composites as Adsorbents for Removal of UO2+2 from Aqueous Solutions. *J. Mol. Liq.* **2015**, *207*, 224–230. https://doi.org/https://doi.org/10.1016/j.molliq.2015.03.044.

(12) Alessi, D. S.; Fein, J. B. Cadmium Adsorption to Mixtures of Soil Components: Testing the Component Additivity Approach. *Chem. Geol.* **2010**, *270* (1–4), 186–195. https://doi.org/10.1016/j.chemgeo.2009.11.016.

(13) Arnold, T.; Zorn, T.; Zänker, H.; Bernhard, G.; Nitsche, H. Sorption Behavior of U(VI) on Phyllite: Experiments and Modeling. In *Journal of Contaminant Hydrology*; 2001; Vol. 47, pp 219–231. https://doi.org/10.1016/S0169-7722(00)00151-0.

(14) Qu, C.; Du, H.; Ma, M.; Chen, W.; Cai, P.; Huang, Q. Pb Sorption on Montmorillonite-Bacteria Composites: A Combination Study by XAFS, ITC and SCM. *Chemosphere* **2018**, *200*, 427–436. https://doi.org/10.1016/j.chemosphere.2018.02.136.

(15) Wang, N.; Du, H.; Huang, Q.; Cai, P.; Rong, X.; Feng, X.; Chen, W. Surface Complexation Modeling of Cd(II) Sorption to Montmorillonite, Bacteria, and Their Composite. *Biogeosciences* **2016**, *13* (19), 5557–5566. https://doi.org/10.5194/bg-13-5557-2016.

(16) Mayordomo, N.; Alonso, U.; Missana, T. Effects of γ-Alumina Nanoparticles on Strontium Sorption in Smectite: Additive Model Approach. *Appl. Geochemistry* **2019**, *100*, 121–130. https://doi.org/10.1016/j.apgeochem.2018.11.012.

(17) Moon, E. M.; Peacock, C. L. Modelling Cu(II) Adsorption to Ferrihydrite and Ferrihydrite-Bacteria Composites: Deviation from Additive Adsorption in the Composite Sorption System. *Geochim. Cosmochim. Acta* **2013**, *104*, 148–164. https://doi.org/10.1016/j.gca.2012.11.030.

(18) Lei, M.; Tao, J.; Yang, R.; Tie, B.; Liu, X.; Wei, X.; Du, H. Binding of Sb(III) by Sb-Tolerant Bacillus Cereus Cell and Cell-Goethite Composite: Implications for Sb Mobility and Fate in Soils and Sediments. *J. Soils Sediments* **2019**, *19* (Iii), 2850–2858. https://doi.org/10.1007/s11368-019-02272-z.

(19) Otero, A.; Peacock, C. L.; Fiol, S.; Antelo, J.; Carvin, B. A Universal Adsorption Behaviour for Cu Uptake by Iron (Hydr)Oxide Organo- Mineral Composites. *Chem. Geol.* **2018**, *479* (December 2017), 22–35. https://doi.org/10.1016/j.chemgeo.2017.12.022.

(20) Qu, C.; Ma, M.; Chen, W.; Cai, P.; Huang, Q. Surface Complexation Modeling of Cu(II) Sorption to Montmorillonite–Bacteria Composites. *Sci. Total Environ.* **2017**, *607–608*, 1408–1418. https://doi.org/10.1016/j.scitotenv.2017.07.068.

(21) Serrano, S.; O'Day, P. A.; Vlassopoulos, D.; García-González, M. T.; Garrido, F. A Surface Complexation and Ion Exchange Model of Pb and Cd Competitive Sorption on Natural Soils. *Geochim. Cosmochim. Acta* **2009**, *73* (3), 543–558. https://doi.org/10.1016/j.gca.2008.11.018.

(22) Lewis, T. M. Sorption of Metals to Clay Minerals in the Presence of Complexing Organic Ligands, Loughborough University, 2008.

(23) Ebong, F. S.; Evans, N. Modelling the Sorption of 63 Ni to Granitic Materials: Application of the Component Additive Model. *J. Environ. Sci. Eng. B 1* **2012**, 281–292.

(24) Gustafsson, J. P. Modelling Competitive Anion Adsorption on Oxide Minerals and an Allophane-Containing Soil. *Eur. J. Soil Sci.* **2001**, *52* (4), 639–653. https://doi.org/10.1046/j.1365-2389.2001.00414.x.

(25) Dong, W.; Wan, J. Additive Surface Complexation Modeling of Uranium(VI) Adsorption onto Quartz-Sand Dominated Sediments. *Environ. Sci. Technol.* **2014**, *48* (12), 6569–6577. https://doi.org/10.1021/es501782g.

(26) Mourdikoudis, S.; Pallares, R. M.; Thanh, N. T. K. Characterization Techniques for Nanoparticles: Comparison and Complementarity upon Studying Nanoparticle Properties. *Nanoscale* **2018**, *10* (27), 12871–12934. https://doi.org/10.1039/c8nr02278j.

(27) Motuzas, A.; Vaisvalavicius, R.; Prosyčevas, I. Application of New Physical Chemical Methods in Soil Ecological Investigations. *Environ. Sci. Pollut. Res.* **2002**, *9* (S1), 55–62. https://doi.org/10.1007/BF02987427.

(28) Vickerman, J. S.; Gilmore, I. S. *Surface Analysis – The Principal Techniques, 2nd Edition*; John Wiley & Sons, Inc., 2009. https://doi.org/10.1002/9780470721582.

(29) Goebl, D.; Bruckner, B.; Roth, D.; Ahamer, C.; Bauer, P. Low-Energy Ion Scattering: A Quantitative Method? *Nucl. Instruments Methods Phys. Res. Sect. B Beam Interact. with Mater. Atoms* **2015**, *354*, 3–8. https://doi.org/10.1016/j.nimb.2014.11.030.

(30) Cushman, C. V.; Brüner, P.; Zakel, J.; Major, G. H.; Lunt, B. M.; Smith, N. J.; Grehl, T.; Linford, M. R. Low Energy Ion Scattering (LEIS). A Practical Introduction to Its Theory, Instrumentation, and Applications. *Anal. Methods* **2016**, *8* (17), 3419–3439. https://doi.org/10.1039/C6AY00765A.

(31) van Leerdam, G. C. Surface Analysis of Catalysts by Low-Energy Ion Scattering, Eindhoven University of Technology, 1991. https://doi.org/10.6100/IR345264.

(32) Almeida, R. M.; Jain, H.; Pantano, C. G. Low-Energy Ion-Scattering Spectroscopy of Modified Silicate Glasses. *J. Am. Ceram. Soc.* **2016**, *99* (4), 1259–1265. https://doi.org/10.1111/jace.14126.

(33) ter Veen, H. R. J.; Kim, T.; Wachs, I. E.; Brongersma, H. H. Applications of High Sensitivity-Low Energy Ion Scattering (HS-LEIS) in Heterogeneous Catalysis. *Catal. Today* **2009**, *140* (3–4), 197–201. https://doi.org/10.1016/j.cattod.2008.10.012.

(34) Hossain, K.; Hasibuzzaman, M. M.; Himeno, S. Characteristics and Health Effects of Arsenic Exposure in Bangladesh. In *Arsenic Contamination in Asia: Biological Effects and Preventive Measures*; Yamauchi, H., Sun, G., Eds.; Springer Singapore: Singapore, 2019; pp 43–60. https://doi.org/10.1007/978-981-13-2565-6_4.

(35) Zhang, F. S.; Itoh, H. Photocatalytic Oxidation and Removal of Arsenite from Water Using Slag-Iron Oxide-TiO2 Adsorbent. *Chemosphere* **2006**, *65* (1), 125–131. https://doi.org/10.1016/j.chemosphere.2006.02.027.

(36) Coronado, J. M.; Hernández-Alonso, M. D. The Keys of Success: TiO2 as a Benchmark Photocatalyst. In *Design of Advanced Photocatalytic Materials for Energy and Environmental Applications*; Coronado, J. M., Fresno, F., Hernández-Alonso, M. D., Portela, R., Eds.; Springer London: London, 2013; pp 85–101. https://doi.org/10.1007/978-1-4471-5061-9_5.

(37) Bissen, M.; Frimmel, F. H. Arsenic - A Review. Part II: Oxidation of Arsenic and Its Removal in Water Treatment. *Acta Hydrochim. Hydrobiol.* **2003**, *31* (2), 97–107. https://doi.org/10.1002/aheh.200300485.

(38) Bullen, J. C.; Lapinee, C.; Salaün, P.; Vilar, R.; Weiss, D. J. On the Application of Photocatalyst-Sorbent Composite Materials for Arsenic(III) Remediation: Insights from Kinetic Adsorption Modelling. *J. Environ. Chem. Eng.* **2020**, *8* (5). https://doi.org/10.1016/j.jece.2020.104033.

(39) Hafeznezami, S.; Lam, J. R.; Xiang, Y.; Reynolds, M. D.; Davis, J. A.; Lin, T.; Jay, J. A. Arsenic Mobilization in an Oxidizing Alkaline Groundwater: Experimental Studies, Comparison and Optimization of Geochemical Modeling Parameters. *Appl. Geochemistry* **2016**, *72* (January 2001), 97–112. https://doi.org/10.1016/j.apgeochem.2016.07.011.

(40) Kanematsu, M.; Young, T. M.; Fukushi, K.; Green, P. G.; Darby, J. L. Arsenic(III, V) Adsorption on a Goethite-Based Adsorbent in the Presence of Major Co-Existing Ions: Modeling Competitive Adsorption Consistent with Spectroscopic and Molecular Evidence. *Geochim. Cosmochim. Acta* **2013**, *106*, 404–428. https://doi.org/10.1016/j.gca.2012.09.055.

(41) Kanematsu, M.; Young, T. M.; Fukushi, K.; Green, P. G.; Darby, J. L. Extended Triple Layer Modeling of Arsenate and Phosphate Adsorption on a Goethite-Based Granular Porous Adsorbent. *Environ. Sci. Technol.* **2010**, *44* (9), 3388–3394. https://doi.org/10.1021/es903658h.

(42) Liu, K.; Fu, H.; Shi, K.; Xiao, F.; Jing, L.; Xin, B. Preparation of Large-Pore Mesoporous Nanocrystalline TiO2 Thin Films with Tailored Pore Diameters. *J. Phys. Chem. B* **2005**, *109* (40), 18719–18722. https://doi.org/10.1021/jp054546p.

(43) BAYOXIDE® E 33 - Liquid Purification Technologies http://lpt.lanxess.com/en/products-lpt/product-groups/iron-oxide-adsorber/bayoxide-product-detail/bayoxider-e-33/ (accessed Jun 15, 2017).

(44) Lützenkirchen, J.; Preočanin, T.; Kovačević, D.; Tomišić, V.; Lövgren, L.; Kallay, N. Potentiometric Titrations as a Tool for Surface Charge Determination. *Croat. Chem. acta* **2012**, *85* (4), 391–417. https://doi.org/10.5562/cca2062.

(45) Stumm, W.; Morgan, J. J. *Aquatic Chemistry*; John Wiley & Sons, Inc., 1996.

(46) Ferguson, M. A.; Hoffmann, M. R.; Hering, J. G. TiO2-Photocatalyzed As(III) Oxidation in Aqueous Suspensions: Reaction Kinetics and Effects of Adsorption. *Environ. Sci. Technol.* **2005**, *39* (6), 1880–1886. https://doi.org/10.1021/es048795n.

(47) Lee, H.; Choi, W. Photocatalytic Oxidation of Arsenite in TiO2 Suspension: Kinetics and Mechanisms. *Environ. Sci. Technol.* **2002**, *36* (17), 3872–3878. https://doi.org/10.1021/es0158197.

(48) Sahai, N.; Sverjensky, D. A. Evaluation of Internally Consistent Parameters for the Triple-Layer Model by the Systematic Analysis of Oxide Surface Titration Data. *Geochim. Cosmochim. Acta* **1997**, *61* (14), 2801–2826. https://doi.org/10.1016/S0016-7037(97)00128-2.

(49) Kanematsu, M.; Young, T. M.; Fukushi, K.; Green, P. G.; Darby, J. L. Extended Triple Layer Modeling Arsenate Adsorption on a Nanostructured Goethite-Based Granular Porous Adsorbent in the Presence of Major Co-Existing Ions. *Abstr. Pap. Am. Chem. Soc.* **2011**, *241* (9), 3388–3394.

(50) Jonsson, C. M.; Jonsson, C. L.; Estrada, C.; Sverjensky, D. A.; Cleaves, H. J.; Hazen, R. M. Adsorption of L-Aspartate to Rutile (α-TiO2): Experimental and Theoretical Surface Complexation Studies. *Geochim. Cosmochim. Acta* **2010**, *74* (8), 2356–2367. https://doi.org/10.1016/j.gca.2010.01.003.

(51) Sverjensky, D. A. Prediction of Surface Charge on Oxides in Salt Solutions: Revisions for 1:1 (M+L-) Electrolytes. *Geochim. Cosmochim. Acta* **2005**, *69* (2), 225–257. https://doi.org/10.1016/j.gca.2004.05.040.

(52) Jonsson, C. M.; Jonsson, C. L.; Sverjensky, D. A.; Cleaves, H. J.; Hazen, R. M. Attachment of L-Glutamate to Rutile (r-TiO2): A Potentiometric, Adsorption, and Surface Complexation Study. *Langmuir* **2009**, *25* (20), 12127–12135. https://doi.org/https://doi.org/10.1021/la901635t.

(53) Sverjensky Sahai, N., D. A. Theoretical Prediciton of Single-Site Surface Protonation Equilibrium Constants for Oxides and Silicates in Water. *Geochim. Cosmochim. Acta* **1996**, *60* (1), 3773–3798.

(54) Dixit, S.; Hering, J. Comparison of Arsenic(V) and Arsenic(III) Sorption onto Iron Oxide Minerals: Implications for Arsenic Mobility. *Environ. Sci. Technol.* **2003**, *37* (18), 4182–4189. https://doi.org/10.1021/es030309t.

(55) Schecher, W. D.; McAvoy, D. C. *MINEQL+ V.4.5 Users Manual*; Hallowell, 1998.

(56) Westall, J. *FITEQL: A Computer Program for Determination of Chemical Equilibrium Constants from Empirical Data*; 1982.

(57) Bullen, J. C. Arsenic adsorption modelling: TiO2, Fe2O3 and composite TiO2-Fe2O3 sorbents - detailed characterisation and adsorption data sets http://www.doi.org/10.5281/zenodo.3689692. https://doi.org/10.5281/zenodo.3689692.

(58) Thommes, M.; Kaneko, K.; Neimark, A. V.; Olivier, J. P.; Rodriguez-Reinoso, F.; Rouquerol, J.; Sing, K. S. W. Physisorption of Gases, with Special Reference to the Evaluation of Surface Area and Pore Size Distribution (IUPAC Technical Report). *Pure Appl. Chem.* **2015**, *87* (9–10), 1051–1069. https://doi.org/10.1515/pac-2014-1117.

(59) Sotomayor, F. J.; Cychosz, K. A.; Thommes, M. Characterization of Micro/Mesoporous Materials by Physisorption: Concepts and Case Studies. *Acc. Mater. Surf. Res* **2018**, *3* (2), 34–50.

(60) Kosmulski, M. Isoelectric Points and Points of Zero Charge of Metal (Hydr)Oxides: 50 Years after Parks' Review. *Adv. Colloid Interface Sci.* **2016**, *238*, 1–61. https://doi.org/10.1016/j.cis.2016.10.005.

(61) Kosmulski, M. The Significance of the Difference in the Point of Zero Charge between Rutile and Anatase. *Adv. Colloid Interface Sci.* **2002**, *99* (3), 255–264. https://doi.org/10.1016/S0001-8686(02)00080-5.

(62) Ayawei, N.; Ebelegi, A. N.; Wankasi, D. Modelling and Interpretation of Adsorption Isotherms. *J. Chem.* **2017**, *2017*. https://doi.org/10.1155/2017/3039817.

(63) Batool, F.; Akbar, J.; Iqbal, S.; Noreen, S.; Bukhari, S. N. A. Study of Isothermal, Kinetic, and Thermodynamic Parameters for Adsorption of Cadmium: An Overview of Linear and Nonlinear Approach and Error Analysis. *Bioinorg. Chem. Appl.* **2018**, *2018*. https://doi.org/10.1155/2018/3463724.

(64) McArthur, J. M.; Banerjee, D. M.; Hudson-Edwards, K. A.; Mishra, R.; Purohit, R.; Ravenscroft, P.; Cronin, A.; Howarth, R. J.; Chatterjee, A.; Talukder, T.; et al. Natural Organic Matter in Sedimentary Basins and Its Relation to Arsenic in Anoxic Ground Water: The Example of West Bengal and Its Worldwide Implications. *Appl. Geochemistry* **2004**, *19* (8), 1255–1293. https://doi.org/10.1016/j.apgeochem.2004.02.001.

(65) Raven, K. P.; Jain, A.; Loeppert, R. H. Arsenite and Arsenate Adsorption on Ferrihydrite: Kinetics, Equilibrium, and Adsorption Envelopes. *Env. Sci.Technol.* **1998**, *32* (3), 344–349. https://doi.org/10.1021/es970421p.

(66) Sverjensky, D. A.; Fukushi, K. A Predictive Model (ETLM) for As(III) Adsorption and Surface Speciation on Oxides Consistent with Spectroscopic Data. *Geochim. Cosmochim. Acta* **2006**, *70* (15), 3778–3802. https://doi.org/10.1016/j.gca.2006.05.012.

(67) Morin, G.; Wang, Y.; Ona-Nguema, G.; Juillot, F.; Calas, G.; Menguy, N.; Aubry, E.; Bargar, J. R.; Brown, G. E. EXAFS and HRTEM Evidence for As(III)-Containing Surface Precipitates on Nanocrystalline Magnetite: Implications for as Sequestration. *Langmuir* **2009**, *25* (16), 9119–9128. https://doi.org/10.1021/la900655v.

(68) Jia, Y.; Xu, L.; Fang, Z.; Demopoulos, G. P. Observation of Surface Precipitation of Arsenate on Ferrihydrite. *Environ. Sci. Technol.* **2006**, *40* (10), 3248–3253. https://doi.org/10.1021/es051872+.

(69) Mamindy-Pajany, Y.; Hurel, C.; Marmier, N.; Roméo, M. Arsenic(V) Adsorption from Aqueous Solution onto Goethite, Hematite, Magnetite and Zero-Valent Iron: Effects of PH, Concentration and Reversibility. *Desalination* **2011**, *281* (1), 93–99. https://doi.org/10.1016/j.desal.2011.07.046.

(70) Jeong, Y.; Fan, M.; Singh, S.; Chuang, C.; Saha, B.; Leeuwen, J. H. Van. Evaluation of Iron Oxide and Aluminum Oxide as Potential Arsenic(V) Adsorbents. *Chem. Eng. Process.* **2007**, *46*, 1030–1039. https://doi.org/10.1016/j.cep.2007.05.004.

(71) Lützenkirchen, J.; Behra, P. On the Surface Precipitation Model for Cation Sorption at the (Hydr)Oxide Water Interface. *Aquat. Geochemistry* **1995**, *1* (4), 375–397. https://doi.org/10.1007/BF00702740.

(72) Zhu, H. Y.; Ni, L. A.; Lu, G. Q. Pore-Size-Dependent Equation of State for Multilayer Adsorption in Cylindrical Mesopores. *Langmuir* **1999**, *15* (10), 3632–3641. https://doi.org/10.1021/la981515v.

(73) Fripiat, J. J.; Gatineau, L.; van Damme, H. Multilayer Physical Adsorption on Fractal Surfaces. *Langmuir* **1986**, *2* (5), 562–567. https://doi.org/10.1021/la00071a006.

(74) S. Pantuso, F.; L. Gómez Castro, M.; C. Larregain, C.; Coscarello, E.; J. Aguerre, R. Kinetic Approach to Multilayer Sorption: Equations of Isotherm and Applications. In *Food Engineering*; IntechOpen, 2019. https://doi.org/10.5772/intechopen.82669.

(75) Sverjensky, D. A. Interpretation and Prediction of Triple-Layer Model Capacitances and the Structure of the Oxide-Electrolyte-Water Interface. *Geochim. Cosmochim. Acta* **2001**, *65* (21), 3643–3655. https://doi.org/10.1016/S0016-7037(01)00709-8.

(76) Farley, K. J.; Dzombak, D. A.; Morel, F. M. M. A Surface Precipitation Model for the Sorption of Cations on Metal Oxides. *J. Colloid Interface Sci.* **1985**, *106* (1), 226–242. https://doi.org/10.1016/0021-9797(85)90400-X.

(77) Schmidt, J.; Vogelsberger, W. Dissolution Kinetics of Titanium Dioxide Nanoparticles: The Observation of an Unusual Kinetic Size Effect. *J. Phys. Chem. B* **2006**, *110* (9), 3955–3963. https://doi.org/10.1021/jp0553611.

(78) Cheah, S. F.; Kraemer, S. M.; Cervini-Silva, J.; Sposito, G. Steady-State Dissolution Kinetics of Goethite in the Presence of Desferrioxamine B and Oxalate Ligands: Implications for the Microbial Acquisition of Iron. *Chem. Geol.* **2003**, *198* (1–2), 63–75. https://doi.org/10.1016/S0009-2541(02)00421-7.

(79) Xu, N.; Gao, Y. Characterization of Hematite Dissolution Affected by Oxalate Coating, Kinetics and PH. *Appl. Geochemistry* **2008**, *23* (4), 783–793. https://doi.org/10.1016/j.apgeochem.2007.12.026.

(80) Hu, W.; Xie, J.; Chau, H. W.; Si, B. C. Evaluation of Parameter Uncertainties in Nonlinear Regression Using Microsoft Excel Spreadsheet. *Environ. Syst. Res.* **2015**, *4* (1). https://doi.org/10.1186/s40068-015-0031-4.